Elastic wave velocities, chemistry and modal mineralogy of crustal rocks sampled by the Outokumpu Scientific Drill Hole: evidence from lab measurements and modeling

H. Kern, K. Mengel, K.W. Strauss, T.I. Ivankina, A.N. Nikitin, I.T. Kukkonen

▶ To cite this version:

H. Kern, K. Mengel, K.W. Strauss, T.I. Ivankina, A.N. Nikitin, et al.. Elastic wave velocities, chemistry and modal mineralogy of crustal rocks sampled by the Outokumpu Scientific Drill Hole: evidence from lab measurements and modeling. Physics of the Earth and Planetary Interiors, 2009, 175 (3-4), pp.151. 10.1016/j.pepi.2009.03.009 . hal-00535573

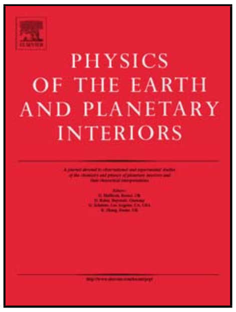

PHYSICS
OF THE EARTH
AND PLANETARY
INTERIORS

Title: Elastic wave velocities, chemistry and modal mineralogy of crustal rocks sampled by the Outokumpu Scientific Drill Hole: evidence from lab measurements and modeling

Authors: H. Kern, K. Mengel, K.W. Strauss, T.I. Ivankina, A.N. Nikitin, I.T. Kukkonen

PII: S0031-9201(09)00063-6
DOI: doi:10.1016/j.pepi.2009.03.009
Reference: PEPI 5157

To appear in: *Physics of the Earth and Planetary Interiors*

Received date: 26-6-2008
Revised date: 11-3-2009
Accepted date: 13-3-2009

Please cite this article as: Kern, H., Mengel, K., Strauss, K.W., Ivankina, T.I., Nikitin, A.N., Kukkonen, I.T., Elastic wave velocities, chemistry and modal mineralogy of crustal rocks sampled by the Outokumpu Scientific Drill Hole: evidence from lab measurements and modeling, *Physics of the Earth and Planetary Interiors* (2008), doi:10.1016/j.pepi.2009.03.009

Elastic wave velocities, chemistry and modal mineralogy of crustal rocks sampled by the Outokumpu Scientific Drill Hole: evidence from lab measurements and modeling

H. Kern[1], K. Mengel[2], K.W. Strauss[2] , T.I. Ivankina[3], A.N. Nikitin[3], I.T. Kukkonen[4]

[1]*Institut für Geowissenschaften, Universität Kiel, 24098 Kiel, Germany*
[2]*Institut für Mineralogie, TU Clausthal, 38678 Clausthal-Zellerfeld, Germany*
[3] *Joint Institute for Nuclear Research, Frank Laboratory of Neutron Physics, 141980 Dubna, Moscow Region, Russia*
[4]*Geological Survey of Finland, Fl-02151 Espoo, Finland*

Abstract: The Outokumpu Scientific Deep Drill Hole intersects a 2500 m deep Precambrian crustal section comprising a 1300 m thick biotite-gneiss series (mica schists) at top, followed by a 200 m thick meta-ophiolite sequence, underlain again by biotite gneisses (mica schists) (500 m thick) with intercalations of amphibolite and meta-pegmatoids (pegmatitic granite). From 2000 m downward the dominating rock types are meta-pegmatoids (pegmatitic granite). Average isotropic intrinsic P- and S-wave velocities and densities of rocks were calculated on the basis of the volume fraction of the constituent minerals and their single crystal properties for 29 core samples covering the depth range 198 m 2491 m. The modal composition of the rocks is obtained from bulk rock (XRF) and mineral chemistry (microprobe), using least squares fitting.

Laboratory seismic measurements on 13 selected samples representing the main lithologies revealed strong anisotropy of P- and S-wave velocities and shear wave splitting. Seismic anisotropy is strongly related to foliation and is, in particular, an important property of the biotite gneisses, which dominate the Upper and Lower gneiss series. At in situ conditions, velocity anisotropy is largely caused by oriented microcracks, which are not completely closed at the pressures corresponding to the relatively shallow depth drilled by the borehole, in addition to crystallographic preferred orientation (CPO) of the phyllosilicates. The contribution of CPO to bulk anisotropy is confirmed by 3D velocity calculations based on neutron diffraction texture measurements. For vertical incidence of the wave train, the in situ velocities derived form the lab measurements are significantly lower than the measured and calculated intrinsic velocities. The experimental results give evidence that the strong reflective nature of the ophiolite-derived rock assemblages is largely affected by oriented microcracks and preferred crystallographic orientation of major minerals, in addition to the lithologic control.

Key words: Outokumpu Deep Drill Hole, modal composition, measured and calculated elastic properties, nature of seismic reflections.

1 Introduction

The Geological Survey of Finland (GTK) has undertaken a deep drilling project in the vicinity of Outokumpu (E Finland) within a Paleoproterozoic metasedimentary and ophiolitic sequence. This project is currently included in the group of ICDP projects. The major goals of the Outokumpu Deep Drilling Project are related to revealing the deep structure of a classical Cu-Co-Zn ore province in Precambrian terrain, the composition and origin of deep saline fluids and gas, investigating the vertical variation of various geophysical and geological parameters and using the open hole as a deep geolaboratory for in situ experiments, fluid sampling and monitoring (for details see Kukkonen and Outokumpu Deep Drilling Working Group, 2007). Drilling commenced in April 2004 and reached its final depth of 2516 m by the end of January 2005. The drilling contractor was the Russian government-owned company NEDRA. The drill hole has been continuously cored with a core diameter of 100 mm. Core recovery was generally higher than 70 %.

One of the aims of the Outokumpu Deep Drilling Project is the investigation of the *in-situ* physical properties of the rocks constituting the 2500 m crustal section penetrated by the bore hole (e.g. seismic velocities, density, porosity as function of P and T; see Kukkonen, 2007, for an update of on-going research in the project).

In this study we will first concentrate on the determination of mineral and chemical composition of representative lithologies in order to arrive at precise modal composition (vol.-%) of the rocks. The bulk composition of rocks, the composition of their constituent minerals and mineral densities are then applied for least squares fit calculation of the modal data.

To characterize the elastic properties of the rocks, we will combine the modal proportions of the rock-forming minerals with the respective single crystal elastic properties for calculating the isotropic intrinsic elastic properties (V_P, V_S, Poisson’s ratio, density), that is, the seismic properties of crack-free samples at room conditions. On a selected number of samples representing major litholgies, we will then measure P- and S-wave velocities in the three foliation-related structural velocities as a function of pressure, in order to investigate the directional dependence (anisotropy) of wave propagation and the effect cracks on velocity and velocity anisotropy at in situ conditions. In addition, we will do 3D numerical velocity calculations based on neutron diffraction texture (CPO) measurements on a number of the strongly anisotropic biotite gneisses, dominating the lithology of the drilled crustal section. CPO-derived velocity surfaces display most distinctly which minerals contribute to the CPO-related intrinsic bulk anisotropy. Finally, we will use the modeled and measured properties to calculate reflection coefficients between and within the main lithological units intersected by the hole and show that anisotropic properties of the meta-sediments are likely very important for generating impedance contrasts between the meta-sediments and other rock types.

2 Geological framework and Outokumpu drilling column

Finland occupies a large part of the Archean and Proterozoic Fennoscandian Shield which is exposed over an area of more than 1 million km^2 (Lehtinen et al., 2005). The drilling site of the Outokumpu Deep Drilling Project is located in the Precambrian area of eastern Finland which is well-known for its Paleoproterozoic ophiolite formations and associated massive Co-Cu-Zn-Ni-sulphide deposits (Vähätalo, 1953; Gaál et al., 1975; Koistinen, 1981; Park, 1988; Sorjonen-Ward, 2006). There are four major lithologic units in the Outokumpu region. (1) The Late Archean Basement is dominated by foliated granitoids and stromatitic migmatites. (2) A thin autochthonous cover sequence records a transition from former terrestrial to passive margin marine sedimentation during rifting events, accompanied by 1.97 to 2.2 Ga old mafic volcanics, sills and dyke swarms. These units are overthrusted by (3) a 2-6 km thick folded and imbricated terrain of monotonous sandy-shaly metaturbidites intercalated with carbo-naceous and sulphidic sandy muds and shales, metamorphosed to amphibolite grade mica-gneisses, mica-schists und black schists. Included in this are ophiolite bodies of serpentinites, 1.95 Ga old gabbros and basalt dykes with marginal selvages in which they grade through carbonate rocks to skarns and quartz-bearing rocks. The combination of serpentinites, carbonate-quartz rock fringes and enclosing sulphidic black schists are known as the Outokumpu rock association forming the host environment of the Outokumpu sulphide ores. (4) Granodioritic to tonalitic intrusions occur as 1.87 to 1.96 Ga old near-concordant sheets. These rocks typically include muscovite and garnet as well as biotite. Figure 1 shows the location of the Outokumpu deep drill hole in Eastern Finland (left) and the lithologies of the 2500 m crustal section penetrated by the borehole (right), as named by the Geological Survey (GTK).

3 Results

A total of 29 core segments covering the depth range from 198 to 2491 m was selected for the present investigation. The length of core samples was generally about 10 cm. In most samples, the foliation (if present) was found to be oriented normal to subnormal to the core (bore hole) axis.

For the bulk and the thin-section analyses, slices have been cut parallel to the core axis so that their orientations were parallel to the lineation (X), if present. The thin sections are in general orientated normal to foliation (X-Z-plane) and parallel to lineation. For investigating the directional dependence of the P- and S-wave propagation (seismic anisotropy), oriented sample cubes (43 mm on edges) were prepared in order to measure Vp and Vs in a triaxial pressure apparatus simultaneously in the three structural directions at elevated pressure conditions. In addition, large-volume pieces of selected biotite gneisses left over from the cube-preparations are used for neutron-diffraction texture analyses with the aim to calculate the 3D velocity distribution of the rocks. The latter investigations were carried out at the Frank Laboratory for Neutron Physics in Dubna (Russia) by means of the SKAT texture diffractometer. Detailed microscopic inspection of the core samples was made to determine the petrographical names of the samples which are more accurate than the working names given for the rock samples during sampling of the core. Figure 2 shows the lithologic column along with the investigated cores and the determined rock names. Sample numbers correspond to the depth of sample recovery.

3.1 Mineralogical and chemical data

3.1.1 Lithology and mineralogy of the 2500 m crustal section

The 2500 m crustal column consists of the following top-to-bottom lithologies:

33 – 1314 m. ***Upper gneiss series:*** strongly foliated fine-grained biotite gneiss. This pile of metasediments is made up by mica schists, biotite gneisses and chlorite-sericite schists.

1314 – 1515 m. *Meta-ophiolite series*: ophiolite-related massive serpentinite with intercalations of weakly foliated graphite-bearing hornblende gneiss and diopside skarn; serpentinites include olivine-tremolite bearing as well as talc-carbonate bearing assemblages. The skarn-rocks include tremolite-bearing serpentinites, tremolite skarn and diopside-tremolite skarn (with and without plagioclase)

1515 – 2013 m. ***Lower gneiss series***: strongly foliated biotite gneiss, intercalated by pyrite and graphite rich hornblende gneiss, metapegmatoids, and amphibolite. The metasediments comprise mica-schists, biotite gneisses and chlorite-sericite schists as well as black schists (calcareous black schists, quartz-rich calcareous black schists, hornblende-epidote schists)

2013 – 2516 m. *Meta-pegmatoid*: coarse grained meta-pegmatoid with a layer of foliated biotite gneiss. The pegmatites include granitic, granodioritic, and tonalitic varieties with varying amounts of muscovite and rare garnet.

In total, the gneisses comprise about 72 %, the serpentinites with intercalations of graphite–bearing gneisses, hornblende gneiss, and skarn rocks about 9 %, and the coarse-grained meta-pegmatiods about 11% of the lithologies constituting the 2500m crustal section. Microphotographs representing the microstructures of the major rock types are shown in Figure 3. They are taken from thin section cut parallel to the XZ plane. They comprise strongly foliated gneisses (a), foliated diopside-skarn (b), massive serpentinite (c) weakly foliated pyrite and grahpite-bearing hornblende gneiss (d), foliated amphibolite (e) and coarse-grained meta-pegmatoids (f).

The strongly foliated biotite-gneisses constituting mainly the upper and lower gneiss series (Fig. 3a) are fine-grained exhibiting strong shape-preferred orientation (SPO) of elongated platy mica grains. Grain sizes of the platy mica minerals vary in length between 0.4 to 2 mm (sub)parallel to X and between 0.4 to 1 mm (sub)parallel to Y. Their width (+/- parallel to Z) is about 5 µm to 200 µm The weakly foliated diopside-skarn (b) of the meta-ophiolite sequence is characterized by strongly heterogeneous grain size distribution: Coarse-grained hornblendes and clinopyroxenes (<1 to 3 mm) are irregularly distributed in a fine-grained matrix of diopside plus hornblende. The massive serpentinite (c) is made up by fine-grained (<1 to 10 µm) platy antigorite and fibrous chrysotile and randomly distributed oxide minerals (magnetite and rare chromite); altered biotite and tremolite grains range from 0.5 to 3 mm. The third component of the meta-ophiolite series is a weakly foliated pyrite and graphite-bearing hornblende-gneiss (d) with an uneven distribution of grain shapes and sizes (0.05 to 2 mm) of quartz, feldspars (oligoclase and orthoclase), and tremolitic amphibole along with randomly distributed pyrite and graphite. The foliated amphibolite (e) intercalated in the lower gneiss series comprises abundant quartz plus andesine of varying grain sizes as well as elongated grains of actinolitic amphibole; pyrite and graphite are disseminated in the rock matrix. The group of meta-pegmatoids (f) in the lower part of the bore hole is dominated by very coarse-grained randomly distributed quartz (0.3 to 8 mm) and feldspar minerals (<1 to 30 mm). Small garnet grains (50 µm to 2 mm) form clusters. A weak shape-preferred orientation of the minor minerals muscovite and biotite is observed only at macroscopic scale. Since these sheet silicates do not occur in every thin section, they were not included in the calculation of modal data from whole rock and mineral microprobe analyses. Their abundance was estimated to be about 2 to 4 vol.-% for muscovite and about 3 vol.-% for biotite.

3.1.2 Bulk chemistry and modal composition

XRF analysis (Philips PW 1480) on Lithium-tetra-borate glass tablets was applied for major elements, except for hydrogen, carbon, and sulfur which were determined together by gravimetry (LOI), if not specified otherwise (S and C by IR spectrometry). Mineral compositions were determined by routine electron microprobe analysis (CAMECA SX 100) with natural minerals standards.

The major element composition (wt.-%) of 29 bulk rock samples is given in Tab. 1, the corresponding microprobe mineral analyses are available upon request. The rocks sampled by the drill hole are felsic and mafic/ultramafic in composition with the felsic types being dominant. The weight percent SiO_2 falls in the range 59 - 73 wt.-% for the biotite gneisses, 75 - 77 wt.-% for the meta-pegmatoids, 55 wt.-% for the diopside skarn, and 38 - 51 wt.-% for the mafic/ultramafic amphibolite and serpentinites.

The modal compositions were calculated from the whole rock major element composition, the number of optically identified minerals, their measured compositions and their densities. The calculation of the mineral modes is based on the generalized petrological mixing model reported by Le Maitre (1979), using the computer program PETMIX which is based on a least squares fit. In contrast to point-counting and Electron Back Scatter Diffraction measurements (EBSD) our approach includes large rock volumes (the bulk core sample), thus providing statistically more reliable results. For instance, a mass of 300 g of rock with an assumed density of 3 g/cm^3 and an average grain size of 1 mm contains about 300 000 grains, which is much more than a few hundred or thousand grains included in point counting and EBDS analyses from thin sections. It should be noted that for strongly foliated rock samples with a marked shape-preferred orientation (SPO) of major minerals, accurate determination of volume percentages by means of point counting and EBDS is difficult, even in case that three perpendicular oriented thin sections are used. This particularly holds for rocks exhibiting, in addition to SPO, pronounced small-scale (mm-size) heterogeneities. In our approach the effects of SPO and small-scale heterogeneities are taken into account. It is fair to say that modal composition data based on point counting and EBSD are accurate as long as the thin section analysis can represent the bulk sample.

The results of the calculated modes for the 29 investigated core samples are listed in Table 2 as volume fractions. Figure 4 displays the variation of the volume fractions of major minerals along the lithologic column, according to the data listed in Table 2. The upper 1300 m thick biotite-gneiss section is largely composed of quartz, plagioclase, biotite and muscovite assemblages varying in the ranges 22 - 48 vol.-%, 20 - 44 vol.-%, 16 – 32 vol.-% and 2 – 17 vol.-%, respectively. In contrast, the biotite gneiss samples collected from the lower gneiss section (1515 - 2013 m depth) are more variable in composition. Alkali feldspar contributes largely to the mode of two samples (22 vol.-% and 28 vol.-%), in addition to quartz, plagioclase, biotite and muscovite.

The core samples recovered from the ophiolitic mafic-ultramafic layers between the upper and lower gneiss section (1314-1515 m depth) are dominated by serpentine (76 – 97 vol.-%) and tremolite (13 vol.-%) in the serpentinites, diopside (72 vol.-%) and amphibole (28 vol.-%) in the skarn, and alkali feldspar (49), hornblende (14 vol.-%), plagioclase (11 vol.-%) and quartz (10 vol.-%) in the hornblende-gneiss. The cores sampled from the meta-pegmatoid section (2013 –2516 m depth) are basically made up by quartz (25 – 35 vol.-%) and plagioclase (41 – 56 vol.-%) and alkali feldspar (7 – 25 vol.-%).

3.2 Elastic wave velocities – calculated and measured

3.2.1 Deriving intrinsic elastic (isotropic) properties from bulk rock and mineral composition

By combining the modal data with the respective velocities of the isotropic monomineralic aggregates of the constituent minerals we calculated the average (isotropic) elastic properties of the rocks according to the formula

.

$$V_{rock} = \sum_{i=1}^{n} Xi \cdot Vi$$

where n is the number of minerals in the aggregate, Xi the volume fraction of each mineral, and Vi the average aggregate velocity of each mineral.

For the calculation, it is important to take into account velocity variations of single minerals with their end-member compositions. Based on the actual mineral composition of the solid-solution minerals plagioclases, alkali-feldspars, clinopyroxenes, and amphiboles determined by microprobe analysis, their velocities were obtained by interpolating between the velocities of the corresponding end-member minerals (Gebrande, 1982), although being aware that wavespeeds of intermediate compositions in a solid solition are not always linearly-interpolatable. The elastic moduli used for the calculation of Vp and Vs of graphite are those of compression-annealed pyrolitic graphite reported by Blakslee (1970). For the calculation of P- and S-wave velocities of the ophiolite-related serpentinites, we used the experimentally determined velocity-density relationship for serpentinite as reported by Watanabe et al. (2007), because single-crystal data of serpentine minerals are not available. Table 3 presents the single crystal velocities (VRH averages) used for the calculation of the average velocities of the rocks. The calculated compressional (V_P) and the shear-wave velocities (V_S) as well as the corresponding Poisson´s ratios and densities are listed in Table 4. The data correspond to the intrinsic isotropic properties, that is, of crack-free and non-porous aggregates. This approach has been successfully applied in earlier investigations (e.g., Mengel 1990; Kern et al, 1996).

3.2.2 *Measuring P- and S-wave velocities and seismic anisotropy as a function of pressure*

On 13 selected samples representing major lithologies we measured P-wave velocities (Vp and S-wave velocities (Vs) and their directional dependence (velocity anisotropy, shear wave splitting) as a function of pressure at room temperature. The experiments were carried out on sample cubes (43 mm edge length) in a multianvil apparatus, allowing simultaneous measurements of Vp and Vs1 and Vs2 in the three structural directions X,Y,Z of the sample cubes and direct determination of length changes (volume change) with increasing pressure and temperature (for details see Kern et al., 1997). Each set of experimental results is composed of 3 P-wave velocities and six S-wave velocities. We used the ultrasonic pulse transmission technique for the velocity measurements with transducers operating at 2 MHz and 1 MHz for P- and S-waves, respectively. The precision of timing measurements is +/- 5ns, and the timing accuracy is assumed to be better than +/- 0.5%.Length and resulting volume changes of the sample cube, due to changes of principal stress, are obtained by the piston displacement.

Measurements were done over a range of pressures up to 600 MPa. In Figure 6 the averages of the three P-wave velocities measured in the three structural directions X, Y, and Z are plotted as a function of pressure for the investigated samples. Most of the samples studied display the well-known initial step increase of velocity with increasing confining pressure. The non-linear rise on the curves is due to progressive closure of microcracks, typically illustrating the pressure sensitivity of P- and S-wave velocities. Linear behavior is approached at a smaller and smaller rate above about 150 MPa marking elastic volume deformation of the compacted aggregate. It is worthy to note that the slopes of serpentinites (samples 1339 and 1414) are markedly different, indicating that the elastic stiffness of crystallographic structure of the serpentine minerals (in particular normal to the sheet plane) is weak compared to the other rock forming minerals (e.g. quartz, feldspar, diopside etc). The highest velocities are found in the diopside skarn and lowest in the serpentinites.

Seismic anisotropy of P- and S-waves, defined by the percent differences between the maximum and minimum velocity with respect to the mean velocity (Birch, 1961) is an important property of most investigated samples. This holds, in particular, for the strongly foliated biotite gneisses dominating the Upper and Lower gneiss series by about 70 % of the lithologic column sampled by the borehole. Another important diagnostic phenomenon for anisotropy is shear wave splitting. Analogous to the birefringence in minerals, it occurs when shear waves propagate through anisotropic materials (Crampin, 1987). A single shear wave is split into two orthogonal polarizations which travel at different velocities in the same direction.

A typical set of experimental data for P- and S-.wave velocities measured in the three structural directions for the biotite gneiss 676 is shown in Figure 7. The diagram documents a close relationship of P- and S-wave velocities and shear wave splitting (S1 – S2) to the structural frame X, Y, and Z. Highest and lowest velocities are measured parallel and normal to foliation, respectively. A very pronounced shear wave splitting is apparent parallel to X and Y within the foliation plane (XY plane) with the fast split shear wave being polarized parallel to foliation. Normal to foliation (parallel to Z) there is practically no shear wave splitting observed. In this direction, the sample behaves quasi-isotropically for shear waves. Figure 8 presents the pressure dependence of velocity anisotropy of P-waves (A-Vp) with increasing pressure for all investigated samples. Anisotropy is almost highest at low pressures due to constructive interference of the effects resulting from oriented microcracks and crystallographic preferred orientation (CPO) of the rock-forming minerals. Increasing pressure reduces the effect of cracks and the residual (intrinsic) anisotropy is mainly due to CPO (e.g. Kern and Wenk, 1990; Ji and Salisbury, 1993). Importantly, the anisotropy continues to decrease slowly over the whole pressure range, obviously due to further crack closure and/or the high degree of compressibility of layered minerals along the c-axis (see Mainprice et al., 2008). The intrinsic anisotropy is highest in the biotite gneisses and lowest in the serpentinites.

The compressional wave velocities (averages of Vp measured in the three structural directions X, Y, and Z) at various confining pressures (room temperature), and corresponding anisotropies are compiled in Table 5. The respective shear wave velocities together with shear wave splitting data (parallel to foliation) are listed in Table 6.

3.2.3 Calculating 3D velocity distribution based on neutron diffraction texture measurements

In order to better understand and interpret the strong intrinsic anisotropy measured on the dominating biotite gneisses, 3D velocity calculations based on neutron diffraction texture measurements were done at the time-of flight (TOF) texture diffractometer at Dubna, Russia (Ullemeyer et al., 1989). Eight core samples collected from the Upper and Lower gneiss series (depth range: 578 – 1093 m and 1609 – 2238 m) were used for the measurements. The high penetration depth of neutrons and the large cross section of the neutron beam at Dubna (5 cm x 8,5 cm) allow the investigation of large volumes of generally coarse-grained geological materials. Importantly, complete pole figures are obtained from a single scan.

Since the biotite gneisses are made up by low symmetry minerals (biotite, quartz and plagioclase) texture analysis of such polyphase rocks is not trivial because of the complex diffraction patterns exhibiting many overlapping peaks (see Xie et. al., 2003; Ivankina et al., 2004). Nevertheless, due to the high resolution of the SKAT diffractometer a sufficient number of not overlapped pole-figures could be extracted from the diffraction spectra by simple integration of the peak intensity after background subtraction. From the experimental pole figures we derived the orientation distribution functions (ODFs), and recalculated the pole figures for the predominant mineral phases applying the WIMF method (Matthies, 2002).

As an example, Figure 9 shows the recalculated pole figure of sample OKU 676. The biotite (001) pole figure shows a strong single maximum normal to the foliation. The poles of the (010)+(100)-planes are concentrated on a great circle parallel to the foliation plane. The CPOs of quartz and plagioclase are also well pronounced but much weaker. The shape of the pole figures for biotite, (muscovite), quartz and plagioclase as well as the degree of crystallographic preferred orientation was found to be similar in all investigated samples. The orientation strength may be defined by the texture index J which measures the sharpness of CPO clustering (Bunge, 1969, 1982; Mainprice and Silver, 1993). J is normalized so that for random fabrics J =1. Table 7 summarizes the texture indices of mineral phases for the investigated eight core samples. It is clear from Table 7, that the preferred orientation of the phyllosilicates (biotite, muscovite) is markedly stronger than the CPO of quartz and plagioclase.

The corresponding elastic properties of the polycrystals were obtained by averaging single crystal properties over the orientation distribution. There are various averaging schemes such as the Voigt and Reuss averages (e.g. Bina and Hellfrich, 1992). They provide upper and lower bounds, assuming uniform strain and uniform stress, respectively, throughout the textured aggregate. We applied the Voigt method in our calculation because it gives the closest agreement between CPO-derived and laboratory seismic velocities measured at high pressure (Seront, et al., 1989) Using the Christoffel transformation, we calculated Vp, Vs1, and Vs2 and anisotropy for P- waves and shear wave splitting. Figure 10 presents the CPO-based calculation of Vp and Vs velocity surfaces for biotite, quartz and plagioclase (100 vol.-%) and the resulting bulk Vp and Vs1-Vs2 (shear wave splitting) for sample OKU 676, according to the volume fractions of the constituent minerals. It is clear from the diagram that the seismic anisotropy of the biotite gneiss is dominated by the biotite preferred orientation. The directions of minimum and maximum Vp as well as directions of minimum and maximum shear wave splitting (Vs1 – Vs2) of the bulk rock correspond to the slow [001] and fast [100] + [010]- directions of the biotite single crystal.

4. Discussion

From Figure 4 it is clear that the modal composition of the rocks and the respective single crystal velocities contribute largely to the variation of elastic wave velocities with depth (Fig.5). Abundant modal hornblende, diopside, garnet and plagioclase increase the P- and S-wave velocities. In general, high contents of quartz, alkali feldspar and phyllosilicates (biotite, muscovite, chlorite, serpentine) reduce the velocities. Close inspection of Figure 5 reveals that the upper and the lower section of the drill hole above and below the meta-ophiolite series have quite similar modeled bulk velocities Vp and Vs. This is explained by the contrasting abundances of alkali-feldspar (akf) and biotite in the upper gneiss and the pegmatoid series: The biotite-rich gneisses are poor in akf and the akf-rich pegmatoids are poor in biotite. The variations in the proportions of biotite versus akf are not reflected in the bulk rock velocities (Vp and Vs) because their average single crystal velocities are similar (Akf: Vp= 5.93 km/s Vs = 3.26 km/s; biotite Vp = 6.01km/s Vs = 3.00 km/s). In samples 1319 (phlog-graph-gneiss) 1497 (Pyr-graph-hbl-gneiss) and 1845 (amphibolite) iron-sulfides as well as graphite contribute to the high velocities. The Poisson´s ratios of the 29 samples vary between 0.216 and 0.319 (Table 4). Abundant modal hornblende, diopside, garnet, plagioclase and, in particular, serpentine, give rise to relatively high Poisson’s values, but greater abundance of quartz lowers the Poisson´s ratio. This is in agreement with earlier findings of Christensen and Fountain (1975), Kern et al.(1991), Kern et al. (1999) and others. Accordingly, we find the lowest Poisson’s value in samples 468, 1251, and 1940, which contain 47.5, 43.6, and 49.2 vol.-% quartz. The highest Poisson’s ratios are observed in the serpentinites of the meta-ophiolite section. Comparison of the mean P-wave velocities measured at 600 MPa and room temperature (Table 5) with the corresponding velocities derived from modal mineralogy (Table 4) reveals fairly good agreement for the biotite gneisses dominating the lithologic column. The correspondence for the ophiolite-related rock assemblages is less pronounced, in particular for the serpentinite. We assume that the single crystal velocities used for the calculation (Blakslee et al.,1970) were probably too high. It is important to note that the two data sets refer to intrinsic properties, that is, to the properties of the rock matrix, ignoring the effect of cracks.

Comparing the intrinsic velocities measured in the three structural directions of three biotite gneisses (OkU 578, 676, 818) for which we also calculated the intrinsic velocities derived from CPOs of major minerals, reveals that the measured velocities are lower (6.12 km/s; 6.18 km/s; 6.11 km/s) compared to 6.37 km/s; 6.34 km/s; 6.33 km/s and that the anisotropy is higher than those inferred from CPO patterns obtained by the neutron diffraction measurements (23.67 %, 13.13 %; 13.8 % compared to 11.6 %; 7.2 %; 7.9 %). A likely explanation for this that in our polyphase averaging neither effects of grain shape and inter-grain spherical pores are taken into account that would lower elastic stiffness and correspondingly acoustic velocities. Furthermore, minor phases were not considered in the calculation. Nevertheless, the measured intrinsic P-wave anisotropy which is nearly the double of the calculated ones, can only in part be explained by preferred mineral orientation (CPO). We therefore suggest that shape preferred orientation (SPO) of the oriented bioitite and muscovite crystals and grain boundary effects contribute also largely to the measured bulk anisotropy. Higher experimental acoustic velocities and lower anisotropies than those inferred from CPO patterns are also reported by Wenk et al. 2008 for clays. It should be noted, however, that self-consistent calculations reported by Mainprice and Humbert (1994) for mica aggregates showed that grain-shape (as presented by an Eshelby elastic inclusion) had very little effect on the seismic anisotropy of aggregates composed of a highly anisotropic mineral like mica, and that CPO was dominant.

The laboratory seismic measurements reveal that elastic wave propagation through the rocks sampled by the bore hole are very sensitive to the state of microfracturing, in addition to changes in mineral composition. Preparation of the sample cubes from the center of the cores ensured that disturbance of the microstructure by drilling was minimized. Thus, it is assumed that the effect of microcracks documented by the non-linear slopes on the velocity vs. pressure curves is only in part due to decompaction as a result of the rapid pressure (and temperature) release during core retrieval. Because the ”crack-closing pressure” indicated by the transition from non-linear to linear behaviour is generally above about 100 MPa, corresponding to a depth of about 3.500 m, we might conclude, that the in situ velocities (and densities) of the 2500 m crustal segment at Outokumpu are also affected by open microcracks. It should be noted, however, that P- and S-wave velocities measured on the Outokumpu core samples refer to dry rocks. Pore content and pore pressure may have an important bearing on the in situ wave velocities. Compared to the air-filled pore spaces in dry rocks, saturation of pore space by water (Ppore = 0) increases Vp, whereas Vs remains unaffected (Nur and Simmons, 1969). In case that pore pressure approaches the lithostatic pressure (Ppore ≅ Plith.), microcracks and grain boundaries are more or less kept open. As a consequence, both P- and S-wave velocities are smaller than in dry rocks, due to a reduction of the effective pressure (Peff. = Plith.-n.Ppore; n ≅ 1).

The seismic laboratory measurements reveal that significant velocity anisotropy is present in most investigated samples. This holds, in particular, for the biotite gneisses which dominate the 2500 m crustal section. Both, P- and S-waves anisotropy as well as shear wave splitting are closely related to foliation. In most samples highest and lowest values are parallel and normal to foliation, respectively. Velocity anisotropy is largely caused by lattice preferred orientation (CPO) of the phyllosilicates and by oriented microcracks, which are not completely closed at the pressures corresponding to the relatively shallow depth range drilled by the borehole. In the biotite gneisses, in particular, microcracks are closely related with the biotite fabric, occurring mainly parallel to the morphologic sheet plane (001). (see Figure 3a). As a result, effects of microfractures and effects of CPO are additive and may thus enhance anisotropy at in situ pressures. Importantly, Vp-anisotropy is significantly higher in dry rocks than in water saturated rocks at atmospheric pressure conditions (Popp and

Kern, 1994). As pressure is increased, differences progressively decrease. The corresponding S-wave velocities and S-wave splitting data are only weakly affected by inter-granular fluids.

The velocity surfaces calculated for the partial fabrics (aggregates; 100 vol.-%) of biotite, quartz, and plagioclase in the biotite gneisses display most distinctly that, compared to quartz and plagioclase, the phyllosilicate (biotite, muscovite) contribute most to the measured intrinsic anisotropy. In addition, the CPO-based modeling of the 3D velocity distribution confirm the close relation of maximum and minimum velocities and shear wave splitting to foliation as observed in the measurements. Because the foliation is almost oriented normal to subnormal to the borehole axis, the indication for strong seismic anisotropy of the Upper and lower biotite gneiss series, when compared to the intercalated meta-ophiolites, suggests that the fabric-related seismic anisotropy of the biotite gneisses may significantly enhance seismic reflections at their contacts to the meta-ophiolite series for vertically incident P- and S-waves. For an assessment of the potential importance of the various lithologic interfaces as seismic reflectors and the role of seismic anisotropy, we calculated the acoustic impedances I (velocity multiplied with density) and the corresponding normal incidence reflection coefficients [$Rc = (I_1 - I_2)/(I_1 + I_2)$]for the various main lithologic contacts, assuming vertical incidence of the wave train. According to Warner (1960), reflection coefficients close to +/-0.1 are required for strong seismic reflections. Table 8 compares the reflection coefficients based on the calculated average velocities derived from the modal mineralogy and single crystal properties of the constituent minerals with those derived from the average velocities obtained by the laboratory seismic measurements for in situ pressure conditions. In addition, we include a calculation based on velocities measured normal to foliation (parallel to the Z direction), taking into account that the foliation of the rocks constituting the 2500 m crustal section is normal to subnormal to the borehole. The data are related to down-hole lithostatic pressures, assuming an average density of 2.75 g/cm^3. From Table 8 it is clear that the experimentally-derived in situ velocities are markedly lower than those calculated from the modal composition of the rocks. The calculated reflection coefficients Rc based on modeled as well as on measured velocities show that negative and positive impedances may cause marked multiple reflections within the meta-ophiolite series, in particular at the contacts of the diopside skarn to serpentinites and serpentinites to the pyr.-

graph.-hbl.gneiss and phlog.graph.-gneiss. Thus, the calculation shows that the differences in the lithologies have the potential to give rise to the strong seismic reflection observed at depths of about 1300m and 1500 m, respectively (see Fig. 1). Moreover, the laboratory seismic measurements simulating in situ conditions indicate that the velocities and impedance of the different lithologies and corresponding reflection coefficients at their contacts are significantly affected by microcracks that are not completely closed, thereby lowering the in situ velocities markedly. From the strong directional dependence of wave propagation in the dominating biotite gneisses, we infer, that seismic reflectivity at their contacts to the ophiolite-related assemblage is significantly enhanced for vertically propagating seismic waves (normal to foliation), due to constructive interference of effects from oriented microcracks and lattice preferred orientation (CPO). It should be noted, however, that the thickness of the lithologic units is critical in any interpretation about reflectivity. A characteristic thickness of observable reflectors is estimated to be about 20 – 200 m (e.g. Parsons et al., 1992). Therefore, the thin amphibolite layer (documented by sample 1845) intercalated in the lower gneiss series at the depth of about 1850 m can probably not be detected by seismic reflection surveys. Figure 11 presents a graph showing P-wave velocity and density in the OKU hole derived from logging data (acoustic sonic log and gamma density log) provided by NEDRA, along with a calculated impedance profile. Comparison with the impedances and reflection coefficients derived form the laboratory seismic measurements and chemistry-based calculated velocities (Table 8) supports our interpretation given above, namely, that the most prominent seismic reflections can be expected at the contacts of the Outokumpu assemblage at 1.3 - 1.5 km with the host rock and within the ophiolitic serpentinite-skarn unit. This particularly holds when the strong seismic anisotropy of the biotite gneisses (mica schists) is included in the interpretation. For vertical incidence of the wave train, the seismic anisotropy of the mica schist will also markedly enhance the impedance contrast at the mica schist/ pegmatitic granite contact, so that seismic reflections may be observable. The spikes of low density and low velocity seen on the logging data of the uppermost 500 m can mostly be attributed to fractures. These conclusions are in agreement with reflection seismic data reported by Kukkonen et al. (2006).

5 Summary and conclusions

The Outokumpu Scientific Drill Hole explored a 2500 m thick section of Precambrian crust. For 29 drill cores covering the depth range 198 – 2491 m we calculated the average intrinsic P-and S-wave velocities and the densities by combining the modal fractions of the constituent minerals with their single crystal velocities and densities. The modal composition of the core samples was derived from the rock major element composition (XRF) and the chemical composition of the optically identified minerals (microprobe) and their densities. On 13 selected samples representing the main lithologies, laboratory seismic measurements were done in the three foliation-related structural directions, in order to determine the in situ properties and to investigate the directional dependence of wave propagation. 3D velocity calculations based on neutron diffraction measurements provided a means to evaluate the relative contribution of the main rock-forming minerals to the bulk anisotropy of the biotite gneisses, dominating the drilled crustal section. Using the data obtained from the various approaches, we arrived at the following conclusions:

1) Calculation of the modal composition of the cores from bulk rock and mineral chemistry using best fit solutions is a powerful alternative to point-counting and EBSD image analysis on thin sections. This holds, in particular, for coarse-grained and foliated rocks exhibiting strong shape (SPO) preferred orientation and small-scale inhomogeneities.

2) Knowledge of the chemical composition of the constituent minerals provide a means to interpolate between the end-member properties of the solid-solution minerals, and thus a more accurate calculation of the whole rock intrinsic (crack-free) velocities and densities.

3) The laboratory seismic measurements give evidence that microfracturing has an important bearing on the in situ velocities. At the pressures corresponding to the relatively shallow depth range drilled by the bore hole, the in situ velocities are markedly lower then the intrinsic velocities, due to the effect of cracks that are not completely closed.

4) From the seismic measurements and CPO-based modeling it is clear that velocity anisotropy is an important property of most investigated rocks, in particular of the biotite gneisses, which dominate

the Upper and Lower gneiss series. Both, the laboratory seismic measurements and the 3D velocity calculations confirm that P- and S-wave anisotropy as well as shear wave splitting are closely related to foliation, with highest and lowest values parallel and normal to it, respectively. Both approaches give evidence that velocity anisotropy is largely caused by crystallographic preferred orientation (CPO), alignment of platy minerals (phyllosilicates) and oriented microcracks.

5) For vertical incidence of the wave train, the alternating layers of serpentinite and diopside- and tremolite-bearing skarn rocks constituting the meta-ophiolite series have the potential to cause the observed strong multiple seismic reflections between 1300 m and 1500 m depth. Importantly, under in situ conditions, velocities and corresponding impedances of the different ligologies are markedly affected by the effect of microfracturing and anisotropy, in addition to the lithologic control. In particular, the strong seismic anisotropy of the biotite gneisses, hosting the ophiolite-related rocks, may enhance seismic reflections at their contacts. This also holds for biotite gneiss/meta-pegmatoid contacts so that seismic reflections are probably observable.

6) Our observations based on laboratory seismic measurements and CPO-based calculations suggest that anisotropy caused by CPO and microstructural characteristics need to be taken into account for the interpretation of seismic data (logging and reflection data as well) at Outokumpu.

Acknowledgments

We appreciate the help of D. Schulte-Kortnack in performing the experiments and of Mrs. G. Reim for technical assistance in preparing figures and diagrams. Ulf Hemmerling is thanked for the preparation of thin sections and A. Fehler for preparing the sample cubes. The critical and constructive reviews by George Helffrich and David Mainprice are greatly appreciated.

References

Blakslee, O.L., Proctor, D.G., Seldin, E.J., Spence, G.B., and Weng, T. (1970). Elastic constants of compression-annealed pyrolitic graphite. J. Appl. Phys.., 41. 3373-3382.

Bina, C.R.and Helffrich, G.R., 1992. Calculation of elastic properties from thermodynamic equation of state principles. Annu. Rev. Earth Planet. Sci, 20, 527-552.

Bunge, H.J., 1969. Mathematische Methoden der Texturanalyse. Akademie-Verlag

Bunge, H.J., 1982. Texture Analysis in Materials Science. Butterworth, London, 599 pp.

Christensen, N. I. and Fountain, D. M. (1975). Constitution of the lower continental crust based on experimental studies of seismic velocities in granulite. Bull. Geol. Soc. Amer., 86, 227-236.

Christensen, N.I. and Szymanski, D.L., 1988. Origin of reflections from the Brevard fault zone. J. Geophys. Res., 93, 1087-1102.

Gaál, G., Koistinen, T., and Mattila, E., 1975. Tectonics and stratigraphy of the vicinity of Outokumpu, North Karelia, Finland: Including a structural analysis of the Outokumpu deposit. Geological Survey of Finland, Bulletin, 271, 67 p.

Gebrande, H.,1982. Elastic wave velocities and constants of elasticity of rock-forming minerals, in *Physical Properties of Rocks*, vol. 1b, edited by G. Angenheister, pp.1-96, Springer-Verlag, New York, 1982.

Hacker, B.R., Abers, G.A. and Peacock, S.M., 2003. Subduction factory, 1. Theoretical mineralogy, densities, seismic wave speeds, and H20 contents. J. Geophys. Soc.. 108, B1, ESE 10-1 – 10-25.

Heikkinen, P., Koivisto, E. and Kukkonen, I.T., 2007. FIRE high resolution seismic survey in Outokumpu. In: Kukkonen, I.T. (ed.), Outokumpu Deep Drilling Project, Second International Workshop, May 21-22, 2007, Espoo, Finland. Programme and Extended Abstracts. Geological Survey of Finland, Southern Finland Office, Marine Geology and Geophysics, Report Q10.2/2007/29, pp. 17-20 (extended abstract).

Horen, H., Zamora, M. and Dubuisson, 1996. Seismic wave velocities and anisotropy in serpentinized peridotites from Xigaze ophiolite: Abundance of serpentinite in slow spreding ridge. Geophys. Res. Lett., 23, 9-12.

Ivankina. T.I., Kern, H. and Nikitin, A.N., 2005. Directional dependence of P- and S-wave propagation and polarization in foliated rocks from the Kola superdeep well: Evidence from laboratory measurements and calculations based on TOF neutron diffraction. Tectonophysics 407, 25-42.

Ivankina, T.I., Kern, H.M. and Nikitin, A.N., 2007. Neutron texture measurements and 3D velocity calculations on strongly foliated biotite gneisses from the Outokumpu Deep Drill Hole. In: Kukkonen, I.T. (ed.), Outokumpu Deep Drilling Project, Second International Workshop, May 21-22, 2007, Espoo, Finland. Programme and Extended Abstracts. Geological Survey of Finland, Southern Finland Office, Marine Geology and Geophysics, Report Q10.2/2007/29, pp. 47-50 (extended abstract).

Kern, H. and Wenk, H.-R., 1990. Fabric-related velocity anisotropy and shear wave splitting in rocks from the Santa Rosa mylonite zone, California, J. Geophys.Res., 95, 11,213-11,223.

Kern, H., Schmidt, R. and Popp, T.,1991. The velocity and density structure of the 4000 m crustal segment at the KTB drilling site and their relationship to lithological and microstructural characteristic of the rocks: an experimental approach. Scientific Drilling, 2, 130-145.

Kern, H., Gao, S. and Liu, Q., 1996. Seismic properties and densities of middle and lower crustal rocks exposed along the North China Geoscience Transect. Earth Planet. Sci. Lett., 139, 439-455.

Kern, H., Gao, S., Jin, Z., Popp, T. and Jin, S.,1999. Petrophysical studies on rocks from the Dabie ultrahigh-pressure (UHP) metamorphic belt, Central China: implication for the composition and delamination of the lower crust. Tectonophysics, 301, 191-215.

Koistinen, T.J., 1981. Structural evolution of an early Proterozoic stratabound Cu-Co-Zn deposit, Outokumpu, Finland. Transactions of the Royal Society of Edinburgh: Earth Sciences 72, 115-158.

Kukkonen, I.T., Heikkinen, P., Ekdahl, E., Hjelt, S.-E., Yliniemi, J., Jalkanen, E. and FIRE Working Group, 2006. Acquisition and geophysical characteristics of reflection seismic data on FIRE transects, Fennoscandian Shield. In: Kukkonen, I.T. and Lahtinen, R. (editors), Finnish Reflection Experiment 2001-2005. Geological Survey of Finland, Special Paper 43, pp. 13-43 +11 appendices.

Kukkonen, I.T. and the Outokumpu Deep Drilling Working Group, 2007. Outokumpu Deep Drilling Project – Introdcution to geology and geophysics of the deep hole and research within the project. In: Kukkonen, I.T. (ed.), Outokumpu Deep Drilling Project, Second International Workshop, May 21-22, 2007, Espoo, Finland. Programme and Extended Abstracts. Geological Survey of Finland, Southern Finland Office, Marine Geology and Geophysics, Report Q10.2/2007/29, pp. 11-16 (extended abstract).

Kukkonen, I.T. (ed.), 2007. Outokumpu Deep Drilling Project, Second International Workshop, May 21-22, 2007, Espoo, Finland. Programme and Extended Abstracts. Geological Survey of Finland, Southern Finland Office, Marine Geology and Geophysics, Report Q10.2/2007/29, 86 p.

Lehtinen, M., Nurmi, P.A. and Rämö, O.T. , 2005 (Eds.), Precambrian Geology of Finland –Key to the Evolution of the Fennoscandian Shield. Elsevier B.V., Amsterdam, 736 p.

Le Maitre, R.W., 1979. A new generalized petrological mixing model. Contr. Mineral. Petrol. 71, 133-137.

Mainprice, D., Le Page, Y., Rodgers, J. and Jouanna, P., 2008. *Ab initio* elastic properties of talc from 0 to 12

GPa: Interpretation of seismic velocities at mantle pressures and prediction of auxetic behaviour at low pressure. Earth and Planetary Science Letters, 274, 327-338.

Mainprice, D. and Humbert, M., 1994. Methods of calculating physical properties from lattice preferred orientation data. Surveys in Geophysics, 15, 575-592.

Mainprice, D. and Silver, P., 1993. Interpretation of SKS-waves using samples from the subcontinental lithosphere. Phys. Earth Planet. Inter. 78, 257-280.

Matthies, S., 2002. 20 years WIMV, History, Experience and Contemporary Developments. Material science Forum 408-412, 95-100.

Mengel, K., 1990. The contribution of xenoliths from the North Hessian Depression to problems of the constitution and evolution of the lower continental crust. Habil. Thesis, Univerisität Göttingen (in German).

Nur, A. and Simmons, G., 1969. The effect of saturation on velocity in low porosity rocks. Earth Planet. Sci. Lett., 7, 183

Park, A.F., 1988. Nature of the Early Proterozoic Outokumpu assemblage, eastern Finland. Precambrian Research 38, 131-146.

Parsons, T., Howie, J.M., and Thomson, G.A., 1992. Seismic constraints on the nature of lower crustal reflectors beneath the extending southern transition zone of the Colorado Plateau, Arizona. J. Geophys. Res. 97, 12,391-12,407.

Popp, T. and Kern, H., 1994. The influence of dry and water saturated cracks on seismic velocities of crustal rocks – a comparison of experimental data with theoretical model., Surveys in Geophysics, 15, 443-465.

Seront, B., Mainprice, D. and Christenesen, N.I., 1989. The complete seismic properties of anorthosite:comparison between CPO and laboratoty measurements. EOS, 70, 460-461.

Sorjonen-Ward, P., 2006. Geological and structural framework and preliminary interpretatio of the FIRE 3 and FIRE 3A reflection seismic profiles, central Finland. In: Kukkonen, I.T. and Lahtinen, R. (editors), Finnish Reflection Experiment 2001-2005. Geological Survey of Finland, Special Paper 43, pp. 105-159.

Ullemeyer, K., Spalthoff, P., Heinitz, J. Isakov, N.N., Nikitin, A.N., Weber, K., 1998. The SKAT texture diffractometer at the pulsed reactor IBR-2 at Dubna: experimental layout and first measurements. Nucl. Instrum. Methods. Phys. Res. A 412/1, 80-88.

Vähätalo, V.O., 1953. On the geology of the Outokumu ore deposit in Finland. Geological Survey of Finland, Bull. 164, 98 p.

Warner, M., 1960. Absolute reflection coefficients from deep seismic reflections. Tectonophysics, 173, 15 – 23.

Watanabe, T., Kasami, H. and Oshima, S. (2007) Compressional and shear wave velocities of serpentinized peridotites up to 200 MPa. Earth, Planets and Space (EPS) 59, 233-244.

Wenk, H.R., Matthies, S., Donovan, J., Chateigner, D., 1998. BEARTEX: a windows-based program system for quantitative texture analysis.. J. Appl. Crystallogr., 31, 362-269.

Wenk, H.-R., Voltolini, M., Mazurek, M. Van Loon, L.R. and Vinsot, A., 2008. Preferred orientations and anisotropy in shales: Callovo-Oxfordian shale (France) and Opalinus clay (Switzerland). Clays and Clay Minerals, 56, 285-306.

Xie, Y., Wenk, H.-R., Matthies, S. 2003). Plagioclase preferred orientation by TOF neutron Diffraction and SEM-EBDSD.

Figure Captions

Fig. 1. Location of the Outokumpu Scientific drill hole and column of the main lithologic units penetrated by the Outokumpu Deep drill hole, along with the GTK nomenclature of the rocks.

Fig. 2. New-named lithiologic column and revised nomenclature for core samples provided by GTK. Sample numbers correspond to sampling depth.

Fig. 3. Microphotographs illustrating typical microstructures of the main rock types (YZ plane). Indicated depths of recovery (m) correspond to sample numbers. Scale: (horizontal edge length) 5.1 mm

a) Strongly foliated biotite gneiss – 318m
b) Foliated diopside skarn – 1388m
c) Massive serpentinite – 1414 m
d) Pyrite and graphite-bearing hornblende gneiss – 1457 m
e) Foliated amphibolite - 1845 m
f) Coarse-grained meta-pegmatoid - 2028m

Fig. 4. Variation of modal composition (vol.-%) of major minerals for the main lithologic units penetrated by the Outokumpu Deep Drill hole.

Fig. 5. Variation of average Vp, Vs, Poisson´s ratio, and density with depth.

Fig. 6. Averages of P-wave velocities measured in the three structural directions X, X, and Z as a function of pressure.

Fig. 7. Directional dependence of P- and S-wave velocities in biotite-gneiss (sample OKU 676) at pressures up to 600 MPa.

Fig. 8. Pressure dependence of P-wave anisotropy A-Vp.

Fig. 9. Recalculated pole figures for biotite, quartz and plagioclase of biotite gneiss OKU 676, based on neutron diffraction texture measurement. Equal area projection. Pole density contours in multiples of random distribution (m.r.d).

Fig. 10. CPO-derived P-wave velocities of the mineral aggregates (100 vol.-%) for biotite, quartz, and plagioclase and calculated velocity surfaces of Vp, and Vs1 – VS2 for the bulk rock (OKU 676), according to the mineral proportions (pie diagram).

Fig. 11.Results of density (kg m^{-3}) and sonic log velocities (m s^{-1}) in the Outokumpu hole together with a calculated profile of acoustic impedance (in units of 10^6 kg m^{-2} s^{-1}).

Tables

Table 1. Sampling depth (sample numbers), lithology and chemical composition (wt.-%) of the investigated core samples of the Outokumpu Deep Drill Hole.

Table 2. Modal compositions (vol.-%) as calculated from wt-% data (see text) along with the calculated bulk densities

Table 3. Velocities and densities of the isotropic aggregates of rock-forming minerals used for the calculation of the bulk rock properties.

Table 4. Calculated elastic properties as derived from modal data and mineral densities (Table 3).

Table 5. Measured compressional wave velocities (km/s) and velocity anisotropies (%) at various confining pressures (20°C) .

Table 6. Measured shear wave velocities and maximum shear wave splitting values (km/s) at various confining pressures (20°C).

Table 7. Texture index J of major minerals of the biotite gneiss samples as derived from polfigures measured by neutron diffraction.

Table 8. Comparison of calculated and measured densities, P-wave velocities and acoustic impedances for the various lithologies and respective reflection coefficients (Rc) at lithologic contacts for vertical incidence of the wave train. Left: calculated (based on modal mineralogy); middle: measured at relevant in situ pressure conditions (referring to average velocities); right: measured at relevant in situ pressure conditions (referring to velocities in the direction normal to foliation (parallel to Z)).

Outokumpu Drilling Results

Lithologic column

Drilling began on April 6, 2004

Mica schist,
black schist interlayers
fracture zones

Strong seismic reflectors

Lithologies of the Outokumpu rock type assemblage:

- *Serpentinite*
- *Skarn rocks*
- *Black schist*

Pegmatitic granite

Fig.1

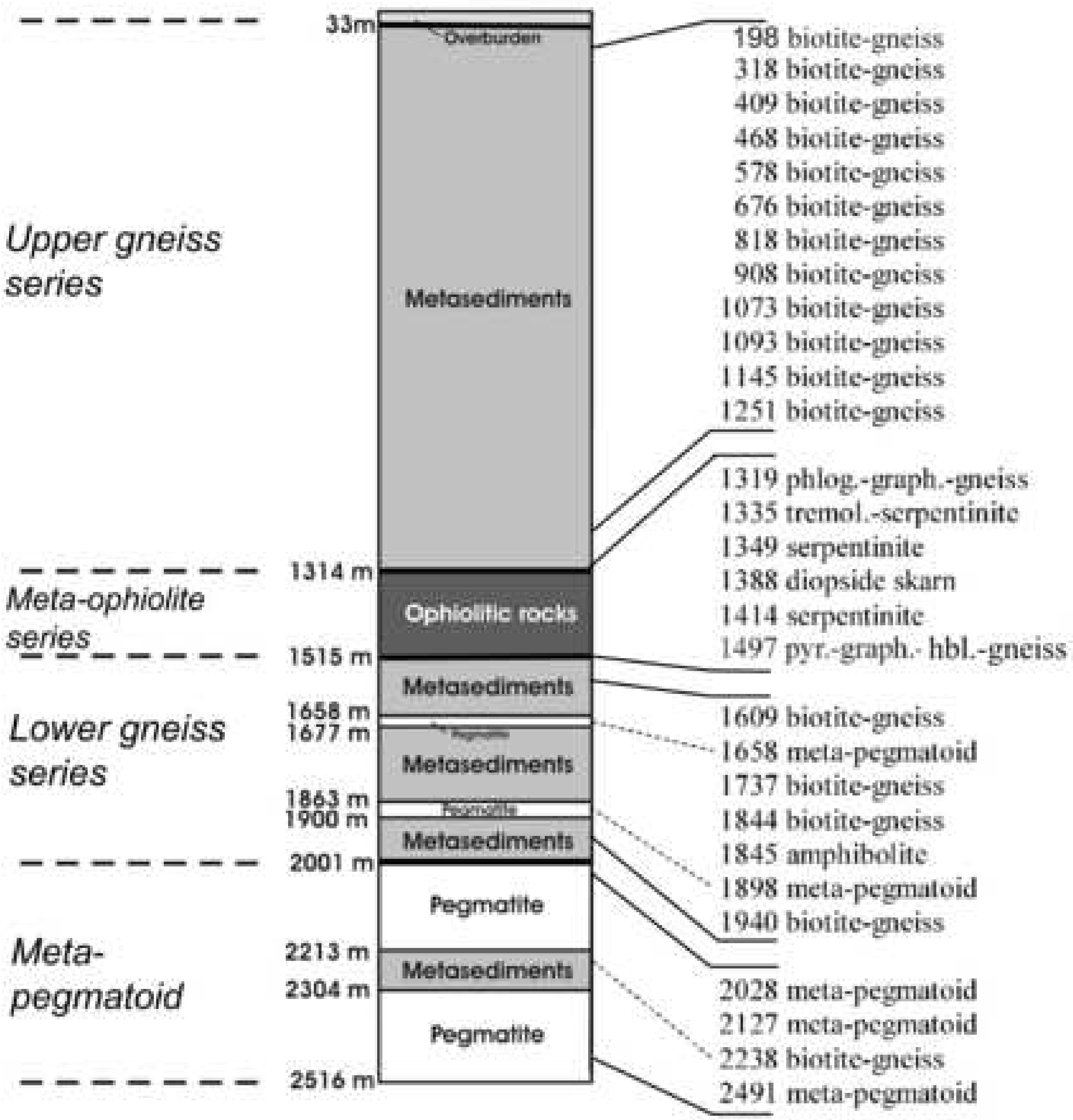

33m
Overburden
Upper gneiss series
Metasediments
1314 m
Meta-ophiolite series
Ophiolitic rocks
1515 m
Metasediments
Lower gneiss series
1658 m
1677 m
Pegmatite
Metasediments
1863 m
1900 m
Pegmatite
Metasediments
2001 m
Meta-pegmatoid
Pegmatite
2213 m
Metasediments
2304 m
Pegmatite
2516 m
198 biotite-gneiss
318 biotite-gneiss
409 biotite-gneiss
468 biotite-gneiss
578 biotite-gneiss
676 biotite-gneiss
818 biotite-gneiss
908 biotite-gneiss
1073 biotite-gneiss
1093 biotite-gneiss
1145 biotite-gneiss
1251 biotite-gneiss
1319 phlog.-graph.-gneiss
1335 tremol.-serpentinite
1349 serpentinite
1388 diopside skarn
1414 serpentinite
1497 pyr.-graph.- hbl.-gneiss
1609 biotite-gneiss
1658 meta-pegmatoid
1737 biotite-gneiss
1844 biotite-gneiss
1845 amphibolite
1898 meta-pegmatoid
1940 biotite-gneiss
2028 meta-pegmatoid
2127 meta-pegmatoid
2238 biotite-gneiss
2491 meta-pegmatoid

Fig.2

Typical microstructures of the main rock types (XZ plane)

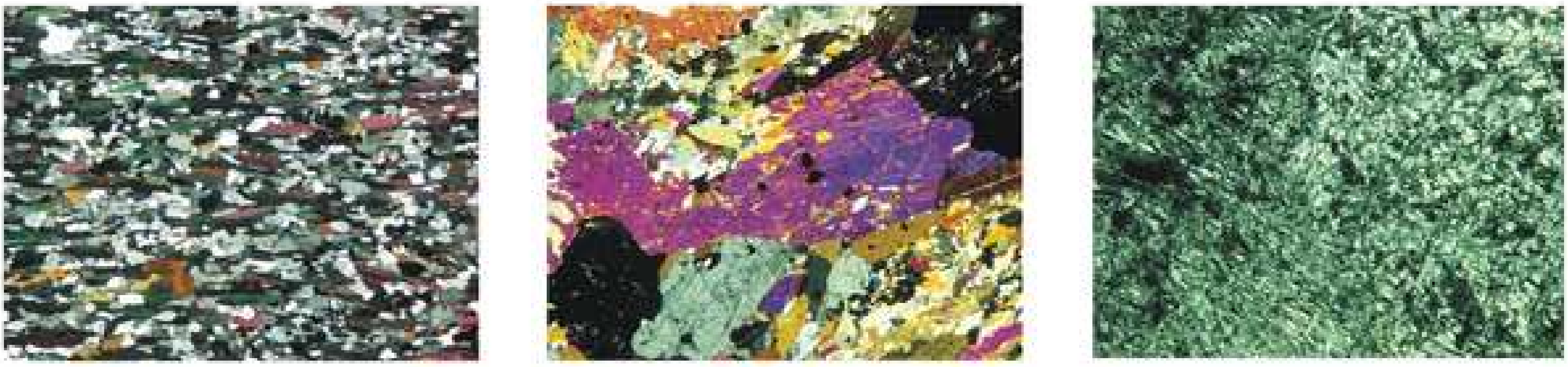

a) Foliated biotite gneiss - 318m

b) Diopside skarn - 1388m

c) Massive serpentine - 1414m

d) Pyr.-graph.-hbl. gneiss - 1497m

e) Foliated amphibolite - 1845m

f) Meta-pegmatoid - 2028m

Scale (horizintal edge): 5.1mm

Fig.3

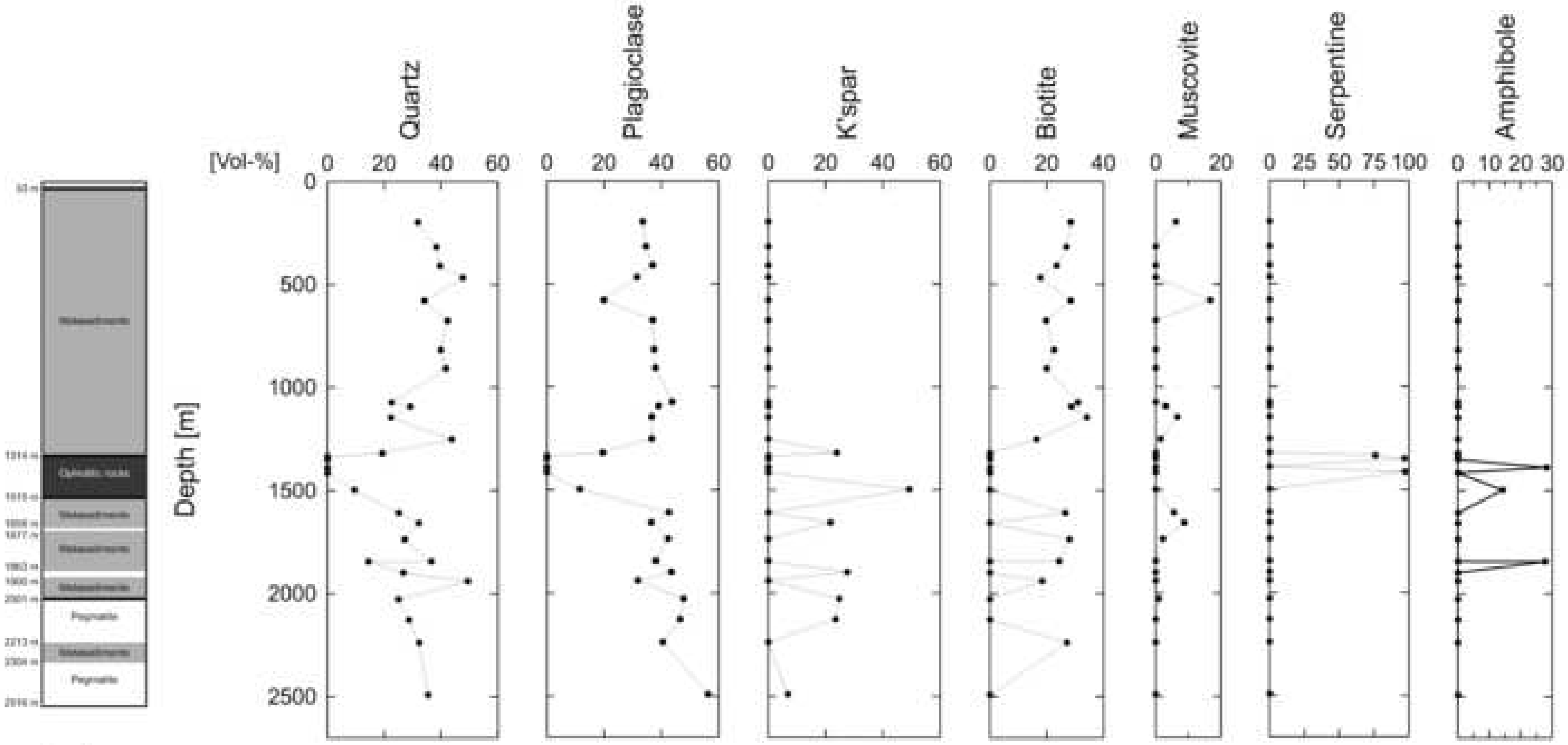
Quartz
Plagioclase
K'spar
Biotite
Muscovite
Serpentine
Amphibole
[Vol-%]
0
20
40
60
25
50
75
100
10
30
Depth [m]
500
1000
1500
2000
2500
50 m
Metasediments
1314 m
Ophiolitic rocks
1515 m
1677 m
1900 m
2001 m
Pegmatite
2213 m
2304 m

Fig. 4

Figure(s)

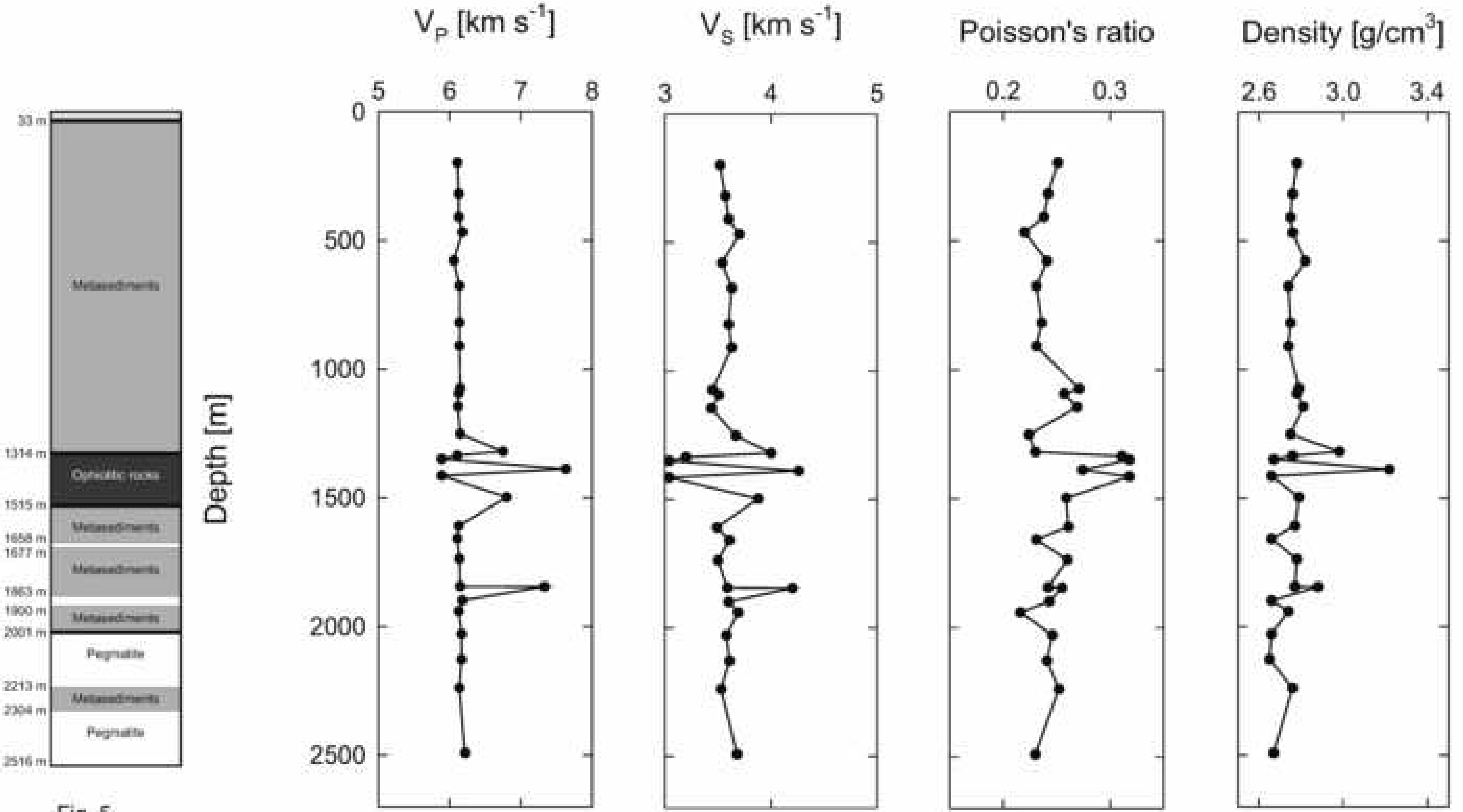

Fig. 5

Figure(s)

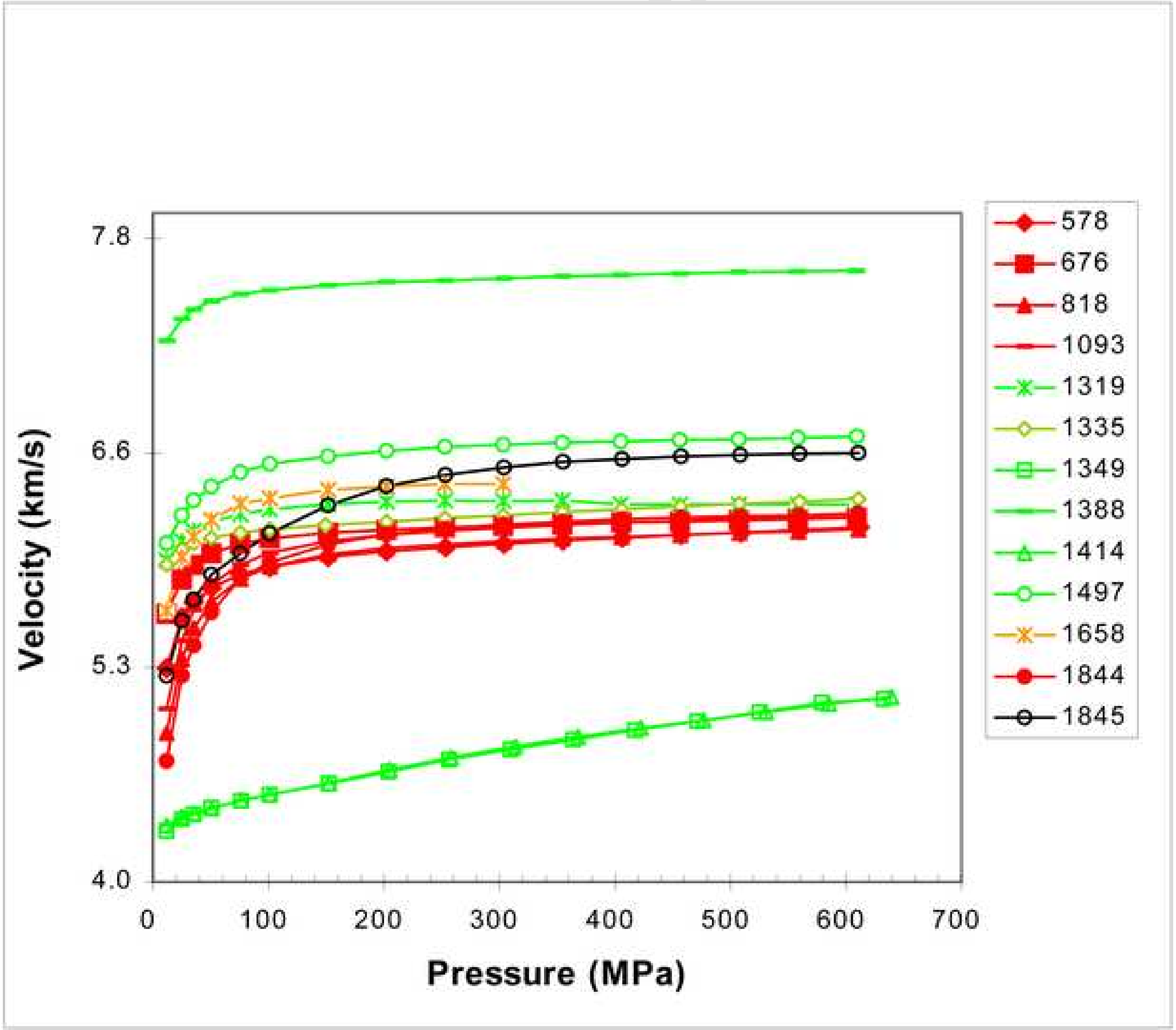

Velocity (km/s)
7.8
6.6
5.3
4.0
0
100
200
300
400
500
600
700
Pressure (MPa)
578
676
818
1093
1319
1335
1349
1388
1414
1497
1658
1844
1845

Figure(s)

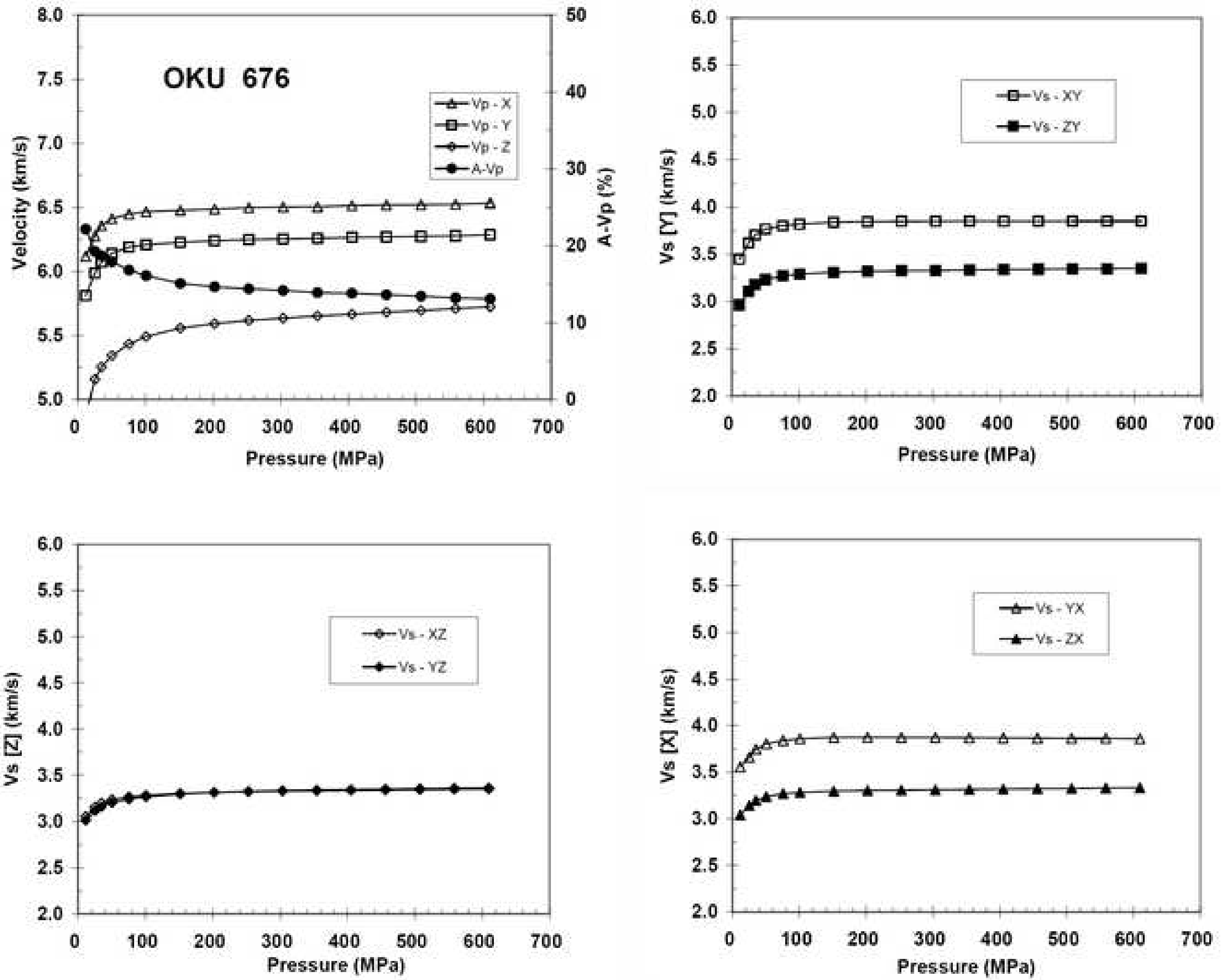
OKU 676
Velocity (km/s)
A-Vp (%)
Pressure (MPa)
Vp - X
Vp - Y
Vp - Z
A-Vp
8.0
7.5
7.0
6.5
6.0
5.5
5.0
50
40
30
20
10
0
0
100
200
300
400
500
600
700
Vs [Y] (km/s)
Vs - XY
Vs - ZY
Vs [Z] (km/s)
Vs - XZ
Vs - YZ
Vs [X] (km/s)
Vs - YX
Vs - ZX
6.0
5.5
5.0
4.5
4.0
3.5
3.0
2.5
2.0

Figure(s)

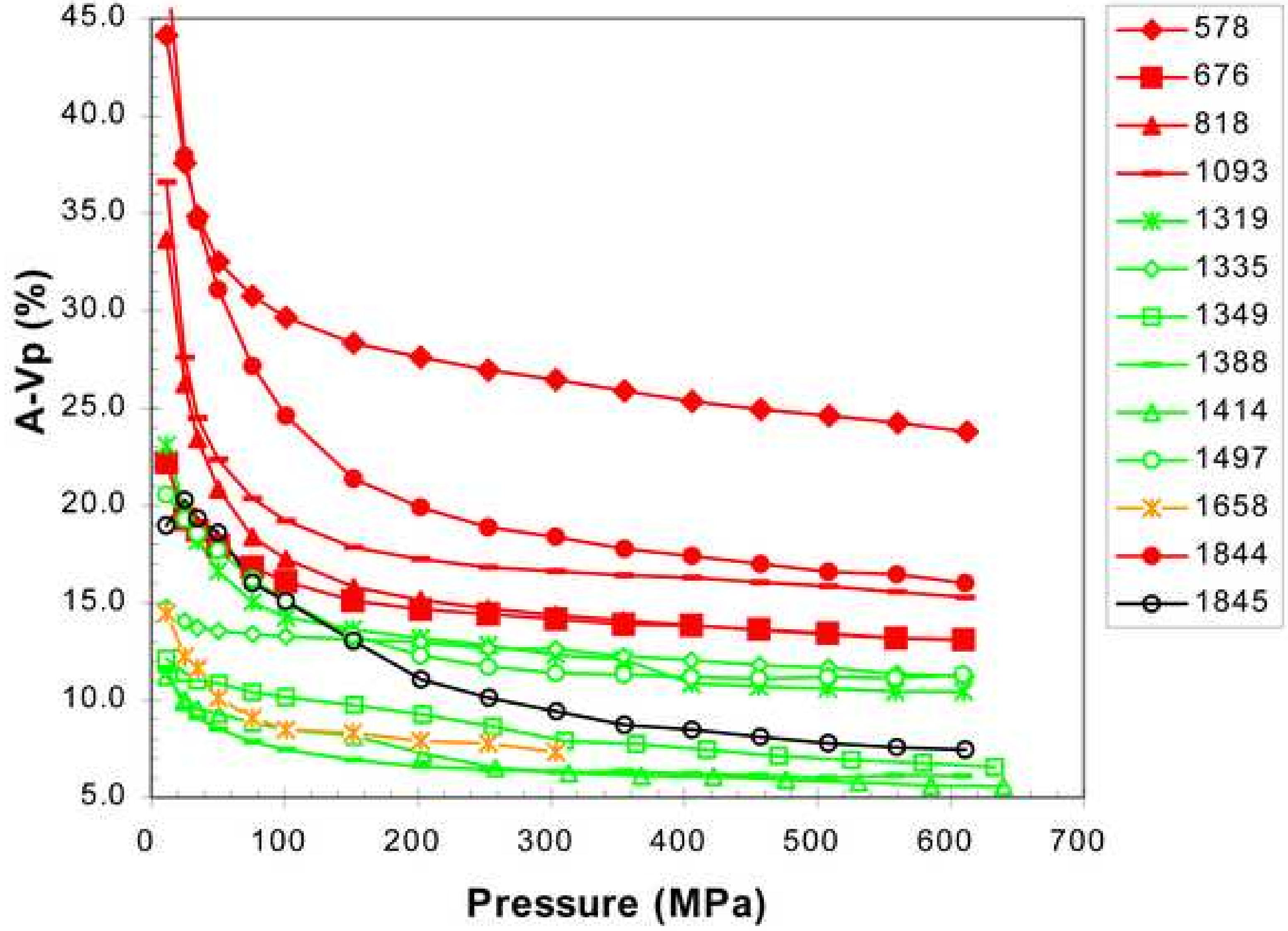
45.0
40.0
35.0
30.0
25.0
20.0
15.0
10.0
5.0
A-Vp (%)
0
100
200
300
400
500
600
700
Pressure (MPa)
578
676
818
1093
1319
1335
1349
1388
1414
1497
1658
1844
1845

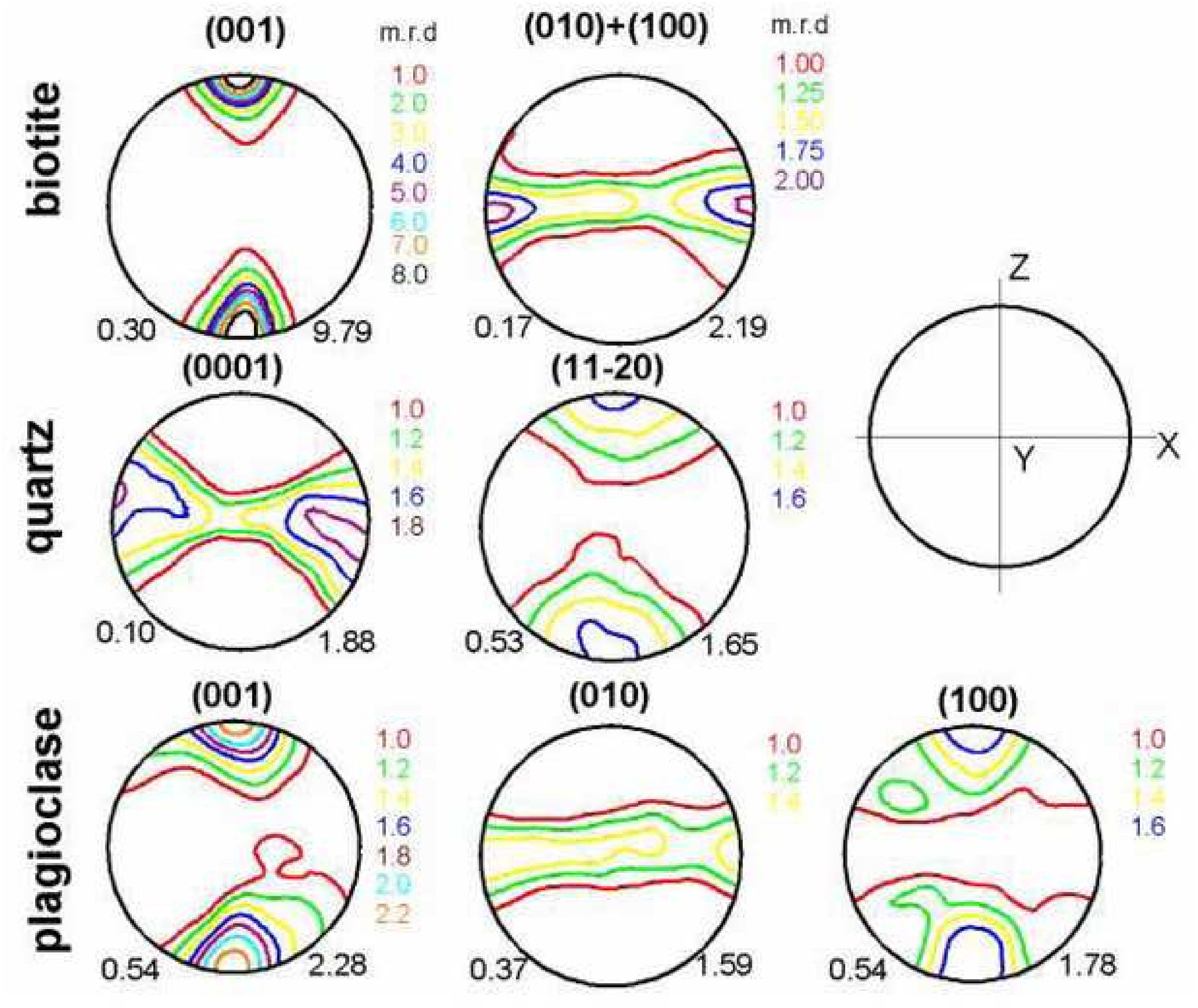
biotite
(001)
m.r.d
1.0
2.0
3.0
4.0
5.0
6.0
7.0
8.0
0.30
9.79
(010)+(100)
m.r.d
1.00
1.25
1.50
1.75
2.00
0.17
2.19
quartz
(0001)
1.0
1.2
1.4
1.6
1.8
0.10
1.88
(11-20)
1.0
1.2
1.4
1.6
0.53
1.65
Z
X
Y
plagioclase
(001)
1.0
1.2
1.4
1.6
1.8
2.0
2.2
0.54
2.28
(010)
1.0
1.2
1.4
0.37
1.59
(100)
1.0
1.2
1.4
1.6
0.54
1.78

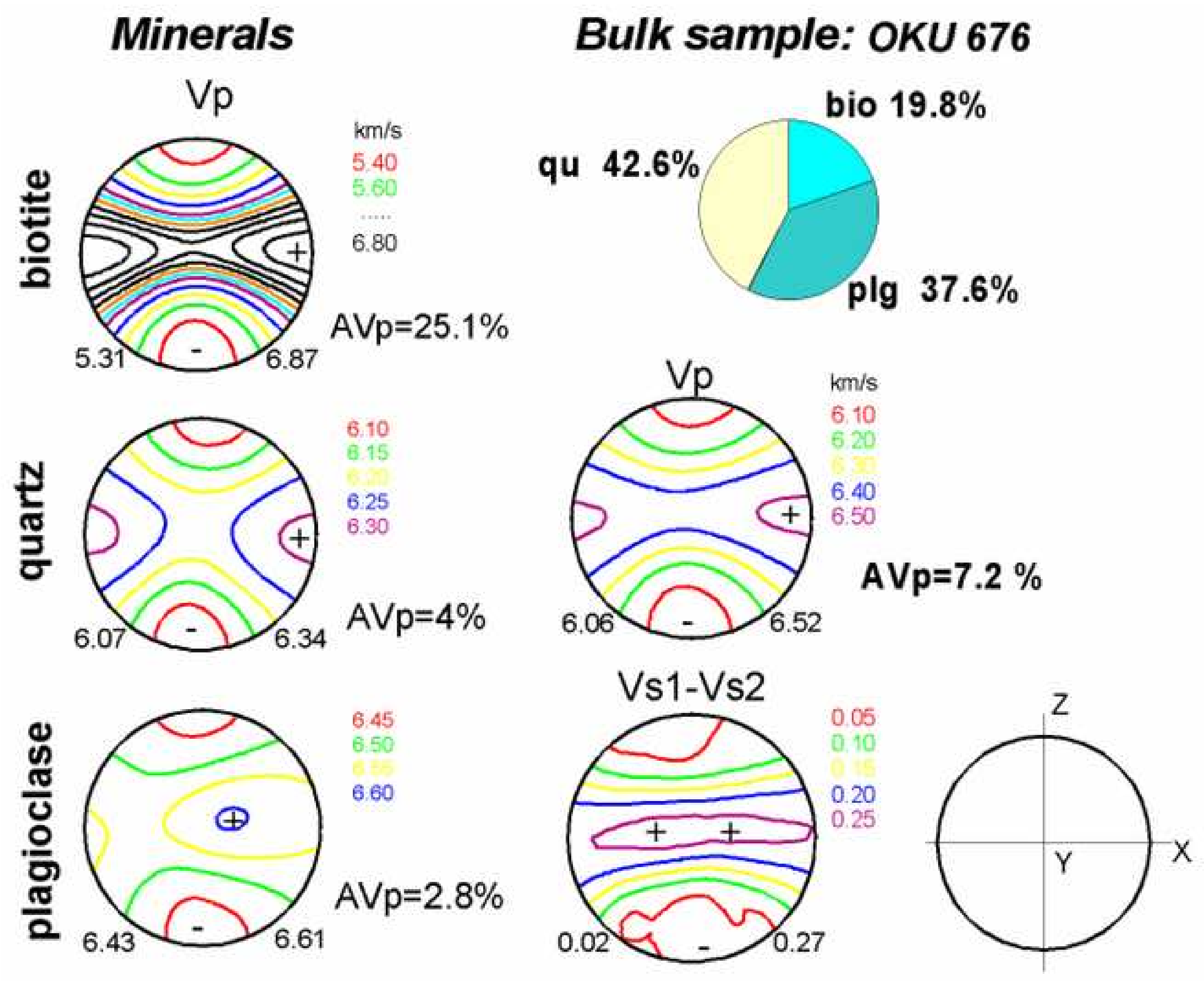
Minerals
Bulk sample: OKU 676
Vp
biotite
km/s
5.40
5.60
......
6.80
AVp=25.1%
5.31
6.87
bio 19.8%
qu 42.6%
plg 37.6%
quartz
6.10
6.15
6.20
6.25
6.30
AVp=4%
6.07
6.34
Vp
km/s
6.10
6.20
6.30
6.40
6.50
AVp=7.2 %
6.06
6.52
plagioclase
6.45
6.50
6.55
6.60
AVp=2.8%
6.43
6.61
Vs1-Vs2
0.05
0.10
0.15
0.20
0.25
0.02
0.27
Z
X
Y

Figure(s)

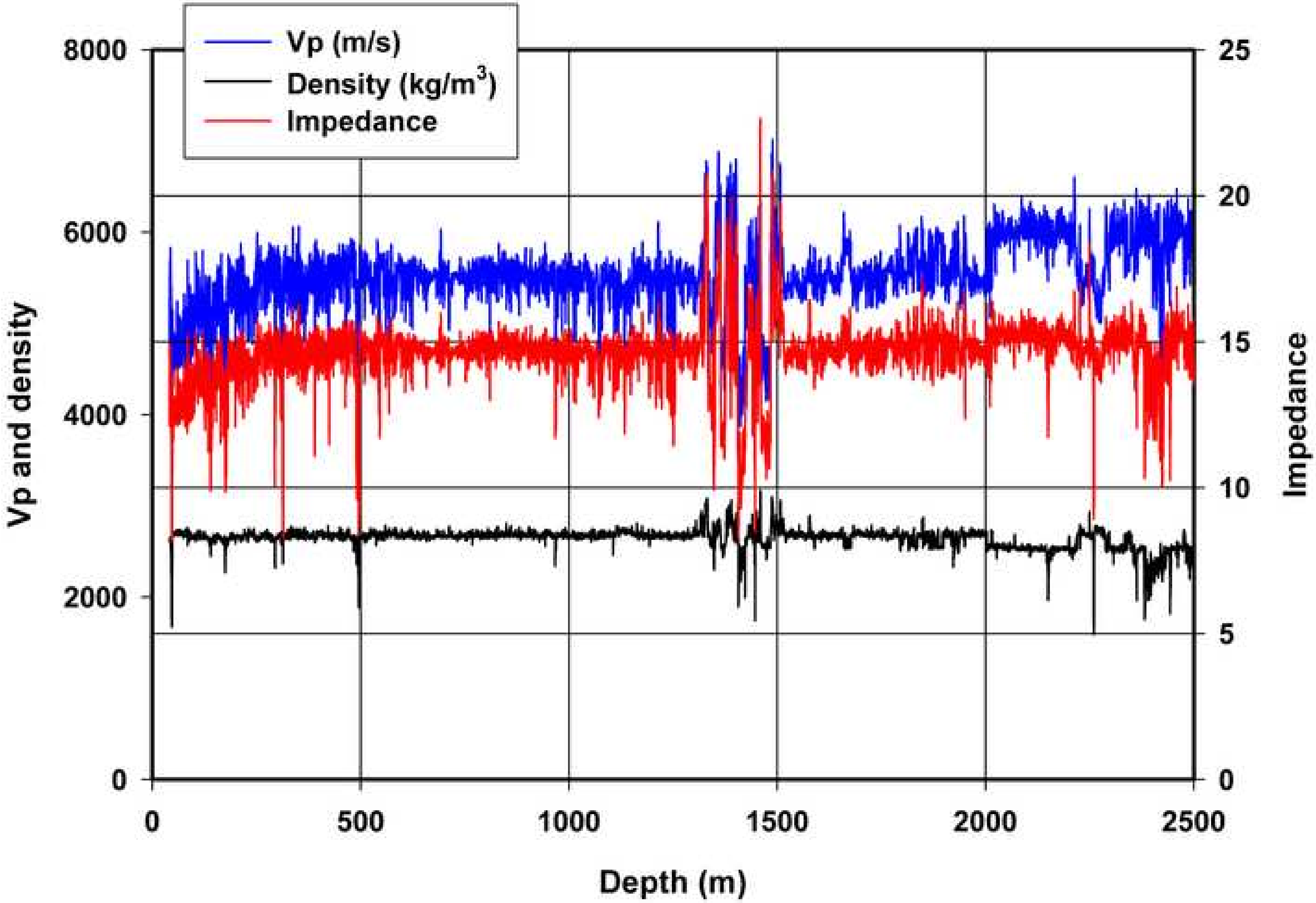
Vp (m/s)
Density (kg/m^3)
Impedance
8000
6000
4000
2000
0
25
20
15
10
5
0
Vp and density
Impedance
0
500
1000
1500
2000
2500
Depth (m)

Table 1. Sampling depth (sample numbers), lithology and chemical composition (wt.-%) of the investigated core sample from the Outokumpu Deep Drill Hole

Depth [m]	**198**	**318**	**409**	**468**	**578**	**676**	**818**	**908**	**1073**	**1093**	**1145**	**1251**	**1319**	**1335**	**1349**
SiO_2	64,86	67,57	69,83	72,70	62,83	70,75	70,16	71,06	60,90	64,96	59,41	71,54	51,77	38,25	37,72
TiO_2	0,79	0,69	0,65	0,59	0,73	0,65	0,64	0,60	0,77	0,72	0,87	0,61	0,50	0,04	0,04
Al_2O_3	15,84	14,51	13,80	12,54	16,93	12,60	13,66	13,45	17,15	15,42	17,87	12,69	11,21	1,02	0,63
FeO	6,31	5,84	5,19	4,67	6,83	4,93	4,98	4,70	7,42	6,27	7,75	4,56	11,46	6,51	7,27
MnO	0,06	0,06	0,05	0,06	0,05	0,07	0,05	0,06	0,08	0,07	0,09	0,06	0,08	0,10	0,06
MgO	2,94	2,69	2,24	1,99	3,34	2,02	2,31	2,12	3,49	3,10	3,62	2,09	1,94	38,60	39,40
CaO	1,61	2,21	1,99	2,52	1,27	2,65	1,90	1,92	2,13	1,56	1,86	2,33	1,13	1,74	0,63
K_2O	3,46	2,60	2,28	1,82	4,31	2,04	2,28	2,04	3,23	3,26	3,99	1,85	5,85	0,02	0,12
Na_2O	2,54	2,90	3,14	1,96	1,50	2,45	2,97	3,14	3,22	3,30	3,02	2,64	1,11	0,00	0,00
P_2O_5	0,16	0,16	0,14	0,16	0,14	0,14	0,15	0,14	0,14	0,14	0,19	0,13	0,14	0,01	0,00
S	0,10												8,24		
C	0,24												6,52		
LOI	1,39	0,76	0,69	0,96	2,04	1,64	0,92	0,78	1,48	1,16	1,33	1,53	12,00	13,1	13,4
$\sum$	99,80	99,82	99,86	99,80	99,83	99,80	99,86	99,88	99,87	99,82	99,81	99,89	99,95	99,37	99,27

Depth [m]	**1388**	**1414**	**1497**	**1609**	**1658**	**1737**	**1844**	**1845**	**1898**	**1940**	**2028**	**2127**	**2238**	**2491**
SiO_2	54,68	37,60	50,45	65,03	75,21	62,87	66,69	45,45	74,75	73,28	74,53	75,93	65,76	76,54
TiO_2	0,02	0,01	0,72	0,69	0,01	0,79	0,68	0,44	0,01	0,56	0,01	0,01	0,64	0,03
Al_2O_3	0,76	0,38	12,88	15,90	14,70	17,00	14,03	12,76	14,98	12,36	15,15	14,12	15,47	14,28
FeO	3,28	7,48	8,13	5,98	0,49	6,45	5,81	8,90	1,01	4,35	0,69	0,61	6,02	0,68
MnO	0,11	0,07	0,04	0,06	0,10	0,06	0,07	0,04	0,28	0,05	0,11	0,02	0,06	0,01
MgO	18,03	40,55	3,37	2,94	0,00	3,00	2,95	5,97	0,00	1,92	0,00	0,00	2,91	0,03
CaO	21,97	0,20	4,82	2,03	0,48	2,21	2,39	7,68	0,51	2,55	0,61	0,91	2,19	1,42
K_2O	0,01	0,01	6,47	3,05	4,21	3,04	2,57	3,70	3,85	1,88	3,94	3,53	2,61	1,14
Na_2O	0,05	0,00	1,07	3,09	4,30	3,46	2,77	0,64	4,21	2,00	4,66	4,56	3,64	5,60
P_2O_5	0,00	0,02	0,09	0,19	0,03	0,18	0,17	0,14	0,03	0,12	0,03	0,01	0,16	0,02
S			5,37					3,81						
C			6,50					10,42						
LOI	0,59	13,8	9,80	1,03	0,50	0,94	1,86	12,67	0,35	0,94	0,29	0,26	0,56	0,29
$\sum$	99,50	100,10	99,81	99,81	99,99	99,81	99,82	99,81	99,97	99,90	99,99	99,95	99,86	100,02

Table 2. Modal compositions in vol.-% as calculated from wt.-% data (see text)

Sample depth	**Qu**	**Plg**	**K-spar**	**Bio**	**Mus**	**Hbl**	**Di**	**Serp**	**Chl**	**Grt**	**IS**	**C**	**Cc**	**Phl**	**Opx**	**Cpx**	**IO**	**Ol**	**Trem**	**Density [gcm^{-3}]**
198	31.9	33.5		28.5	6.2															2.78
318	38.4	34.6		27.0																2.76
409	39.6	36.9		23.4																2.75
468	47.7	31.5		17.8						2.0			1.1							2.76
578	34.1	19.9		28.4	16.7						0.8									2.82
676	42.3	37.0		19.8					0.6		0.3									2.74
818	39.9	37.4		22.6							0.1									2.75
908	41.7	37.9		20.0							0.4									2.74
1073	22.6	43.8		31.0					2.4		0.3									2.79
1093	29.2	39.0		28.7	3.0						0.1									2.78
1145	22.4	36.6		34.2	6.7						0.2									2.81
1251	43.8	36.6		16.4	1.6				0.8		0.9									2.75
1319	19.1	17.7	34.4								10.2	8.2		10.5						2.84
1335								75.9	4.6						0.8	0.8	3.2	1.7	13.0	2.76
1349								96.9									3.1			2.67
1388						28.3	71.7													3.22
1414								97.2									2.8			2.66
1497	9.5	11.5	49.2			14.3					6.7	8.7								2.79
1609	25.1	42.6		26.6	5.6						0.1									2.77
1658	32.2	36.4	21.7		8.7				0.4	0.6										2.66
1737	27.2	42.4		28.0	2.2						0.3									2.78
1844	36.6	38.1		24.4							0.9									2.77
1845	14.4	37.9				27.8					6.6	13.3								2.88
1898	26.7	43.5	27.6							2.2										2.66
1940	49.4	31.8		18.5							0.4									2.74
2028	25.0	47.7	24.8		0.9					1.5										2.66
2127	28.7	46.5	23.5							1.3										2.65
2238	32.3	40.5		27.2																2.76
2491	35.4	56.3	6.8							1.5										2.67

Abbreviations of minerals.Qu=quartz; Plg=plagioclase (An$_{30}$; K-spar = K'feldspar; Bio = biotite; Mus = muscovite; Hbl = hornblende; Di = diopside; Serp = serpentine; Chl = chlorite; Grt = garnet; IS = ironsulfides C = graphite; Cc = calcite; Phl = plogopite; Opx = orthopyroxene; Cpx = clinopyroxene; IO = iron oxides Ol=olivine ; Trem=tremolite .

Table 3. Velocities and densities of the isotropic aggregates of rock-forming minerals used for the calculation of the bulk rock properties

Minerals	V_P [km s^{-1}]	V_S [km s^{-1}]	ρ [g cm^{-3}]
Quartz	6.05	4.09	2.648
Plagioclase	6.30	3.45	2.662
K'feldspar	5.93	3.26	2.555
Biotite	6.01	3.00	3.05
Muscovite	5.81	3.37	2.828
Amphibole	7.20	3.77	3.074
Diopside	7.80	4.45	3.272
Serpentine	5.85	3.00	2.585
Chlorite	6.01	3.00	3.00
Garnet	8.50	4.80	4.324
Fe-sulfides	7.92	5.06	5.01
Graphite	11.64	6.95	2.25
Calcite	6.54	3.43	2.713
Phlogopite	5.62	3.00	2.80
Orthopyroxene	7.03	4.27	3.206
Clinoyroxene	7.70	4.38	3.31
Fe-oxides	6.95	4.2	5.201
Olivine	8.59	5.03	3.22
Tremolite	6.92	3.77	2.979

.

Table 4. Calculated elastic properties and densities as derived from modal data of Table 2

Sample (depth)	V_P [km s^{-1}]	V_S [km s^{-1}]	Poisson's ratio	ρ [g cm^{-3}]
198	6.11	3.52	0.251	2.78
318	6.13	3.57	0.242	2.76
409	6.13	3.60	0.238	2.75
468	6.18	3.70	0.220	2.76
578	6.06	3.54	0.241	2.82
676	6.14	3.63	0.231	2.74
818	6.14	3.60	0.236	2.75
908	6.14	3.63	0.231	2.74
1073	6.15	3.45	0.271	2.79
1093	6.13	3.51	0.257	2.78
1145	6.12	3.44	0.269	2.81
1251	6.15	3.67	0.224	2.75
1319	6.75	4.00	0.230	2.98
1335	6.10	3.19	0.312	2.76
1349	5.93	3.03	0.319	2.67
1388	7.63	4.26	0.274	3.22
1414	5.93	3.03	0.319	2.66
1497	6.80	3.88	0.259	2.79
1609	6.13	3.49	0.261	2.77
1658	6.11	3.61	0.231	2.66
1737	6.14	3.50	0.260	2.78
1844	6.15	3.59	0.242	2.77
1845	7.33	4.20	0.255	2.88
1898	6.18	3.60	0.243	2.66
1940	6.13	3.69	0.216	2.74
2028	6.17	3.58	0.246	2.66
2127	6.17	3.61	0.241	2.65
2238	6.14	3.53	0.252	2.76
2491	6.22	3.68	0.230	2.67

Table 5: Measured compressional wave velocities (km/s) and velocity anisotropy (%) at various pressures (20°C)

Sample	Propagation direction	25 MPa	35 MPa	50 MPa	100 MPa	200 MPa	300 MPa	400 MPa	500 MPa	600 MPa
	X	6.58	6.2	6.65	6.72	6.78	6.8	6.82	6.83	6.85
	Y	5.68	5.77	5.85	5.95	6.02	6.06	6.08	6.11	6.13
	Z	4.48	4.64	4.78	4.98	5.13	5.21	5.28	5.33	5.39
	Mean	5.58	5.68	5.76	5.88	5.98	6.02	6.06	6.09	6.12
	Anis	37.59	34.85	32.52	29.64	27.61	26.47	25.36	24.6	23.79
676	X	6.28	6.36	6.41	6.47	6.49	6.5	6.51	6.52	6.53
	Y	5.99	6.07	6.14	6.21	6.24	6.25	6.26	6.27	6.28
	Z	5.16	5.25	5.34	5.49	5.59	5.63	5.66	5.69	5.71
	Mean	5.81	5.89	5.96	6.06	6.11	6.13	6.15	6.16	6.17
	Anis	19.28	18.72	17.93	16.1	14.45	14.15	13.82	13.43	13.2
818	X	5.6	6.15	6.26	6.42	6.49	6.52	6.53	6.54	6.55
	Y	5.4	5.54	5.67	5.84	5.92	5.95	5.97	5.99	6
	Z	4.6	4.86	5.08	5.4	5.58	5.65	5.69	5.73	5.75
	Mean	5.33	5.52	5.67	5.98	6.01	6.03	6.06	6.09	6.1
	Anis	26.27	23.43	20.83	17.24	15.13	14.36	13.86	13.36	13.2
1093	X	6.15	6.29	6.41	6.54	6.62	6.64	6.67	6.68	6.69
	Y	5.52	5.68	5.82	5.97	6.04	6.08	6.11	6.13	6.19
	Z	4.65	4.91	5.11	5.39	5.57	5.63	5.67	5.7	5.73
	Mean	5.44	5.63	5.78	5.97	6.08	6.12	6.14	6.17	6.19
	Anis	27.59	24.48	22.36	19.19	17.24	16.63	16.29	15.84	15.56
1319	X	6.59	6.62	6.63	6.64	6.65	6.59	6.55	6.55	6.55
	Y	6.14	6.18	6.22	6.29	6.32	6.34	6.34	6.34	6.34
	Z	5.4	5.51	5.61	5.75	5.83	5.86	5.88	5.89	5.9
	Mean	6.04	6.1	6.15	6.23	6.27	6.27	6.27	6.27	6.27
	Anis	19.71	18.2	16.63	14.25	13.17	12.35	10.86	10.59	10.43
1335	X	6.44	6.47	6.5	6.55	6.6	6.62	6.65	6.67	6.69
	Y	5.92	5.96	5.99	6.03	6.07	6.1	6.14	6.17	6.2
	Z	5.6	5.64	5.68	5.74	5.8	5.84	5.9	5.94	5.98
	Mean	5.99	6.03	6.06	6.11	6.16	6.19	6.23	6.26	6.29
	Anis	14.05	13.74	13.55	13.27	12.98	12.62	12.05	11.68	11.24
1349	X	4.42	4.45	4.49	4.57	4.71	4.84	4.95	5.06	5.12
	Y	4.6	4.62	4.66	4.73	4.85	4.95	5.05	5.14	5.23
	Z	4.1	4.14	4.18	4.27	4.42	4.57	4.69	4.78	4.9
	Mean	4.37	4.4	4.44	4.52	4.66	4.78	4.89	4.99	5.08
	Anis	11.4	11.04	10.84	10.15	9.25	7.8	7.55	7.04	6.66
1388	X	7.65	7.71	7.75	7.79	7.81	7.82	7.84	7.85	7.87
	Y	7.5	7.54	7.56	7.6	7.65	7.66	7.67	7.68	7.69
	Z	6.95	7.03	7.11	7.22	7.31	7.34	7.37	7.39	7.41
	Mean	7.37	7.43	7.47	7.54	7.59	7.61	7.62	7.63	7.65
	Anis	9.57	9.09	8.5	7.47	6.61	6.31	6.24	6.04	6.08

Table 5 continued

Sample	Propagation direction	25 MPa	35 MPa	50 MPa	100 MPa	200 MPa	300 MPa	400 MPa	500 MPa	600 MPa
1414	X	4.47	4.45	4.48	4.56	4.71	4.84	4.94	5.05	5.14
	Y	4.57	4.6	4.63	4.69	4.82	4.93	5.01	5.11	5.2
	Z	4.13	4.18	4.22	4.31	4.48	4.63	4.73	4.83	4.92
	Mean	4.39	4.41	4.44	4.52	4.67	4.79	4.9	4.98	5.08
	Anis	10.04	9.55	9.32	8.46	7.24	6.26	6.08	5.8	5.6
1497	X	6.77	6.86	6.92	7	7.01	7.02	7.04	7.06	7.08
	Y	6.23	6.3	6.38	6.47	6.52	6.55	6.57	6.57	6.58
	Z	5.58	5.69	5.79	6.02	6.2	6.27	6.3	6.31	6.33
	Mean	6.19	6.28	6.36	6.5	6.58	6.61	6.63	6.65	6.66
	Anis	19.37	18.56	17.7	1511	12.3	11.4	11.17	11.18	11.2
1658	X	6.01	6.1	6.11	6.27	6.32	6.34			
	Y	6.34	6.46	6.51	6.57	6.64	6.64			
	Z	5.61	5.75	5.87	6.04	6.13	6.17			
	Mean	5.99	6.11	6.17	6.29	6.36	6.38			
	Anis	12.15	11.56	10.12	8.5	7.91	7.35			
1845	X	6.15	6.27	6.4	6.53	6.74	6.82	6.84	6.85	6.86
	Y	5.52	5.63	5.8	6.11	6.34	6.43	6.46	6.47	6.48
	Y	5.02	5.17	5.31	5.61	5.99	6.2	6.29	6.34	6.37
	Mean	5.56	5.69	5.84	6.08	6.41	6.48	6.53	6.55	6.57
	Anis	20.28	19.34	18.59	15.08	11.7	9.41	8.49	7.78	6.58
1844	X	6.02	6.17	6.32	6.51	6.58	6.61	6.62	6.63	6.63
	Y	5.64	5.79	5.94	6.17	6.28	6.31	6.34	6.34	6.35
	Z	4.04	4.29	4.57	5.05	5.38	5.49	5.55	5.6	5.64
	Mean	5.23	5.42	5.61	5.91	6.08	6.14	6.17	6.19	6.21
	Anis	37.94	34.61	31.08	24.62	18.89	18.37	17.4	16.6	16.03

Table 6: measured shear wave velocities (km/s) and maximum shear wave splitting (km/s) at various pressures (20°C)

Sample	Propagation direction	25 MPa	35 MPa	50 MPa	100 MPa	200 MPa	300 MPa	400 MPa	500 MPa	600 MPa
578	X	3.32	3.37	3.4	3.46	3.48	3.49	3.51	3.51	3.52
	Y	3.24	3.32	3.38	3.44	3.48	3.5	3.52	3.53	3.54
	Z	2.98	3.04	3.08	3.15	3.2	3.22	3.24	3.26	3.27
	Mean	3.19	3.25	3.29	3.35	3.39	3.41	3.42	3.43	3.45
	dVs//Fol	1.03	1.06	1.08	1.1	1.07	1.05	1.03	1.01	0.99
676	X	3.4	3.47	3.52	3.57	3.59	3.6	3.59	3.59	3.6
	Y	3.36	3.34	3.5	3.55	3.58	3.59	3.59	3.6	3.6
	Z	3.13	3.18	3.22	3.27	3.31	3.33	3.34	3.35	3.36
	Mean	3.3	3.36	3.41	3.47	3.49	3.5	3.51	3.51	3.52
	dVs//Fol	0.52	0.55	0.56	0.57	0.57	0.56	0.55	0.54	0.53
818	X	3.48	3.57	3.66	3.73	3.82	3.84	3.84	3.84	3.84
	Y	3.08	3.21	3.32	3.47	3.56	3.57	3.58	3.59	3.6
	Z	2.99	3.1	3.19	3.32	3.4	3.42	3.44	3.45	3.46
	Mean	3.18	3.29	3.38	3.51	3.59	3.61	3.62	3.63	3.63
	dVs//Fol	0.36	0.32	0.29	0.28	0.3	0.31	0.3	0.3	0.3
1093	X	3.2	3.31	3.4	3.49	3.53	3.53	3.54	3.54	3.55
	Y	3.14	3.27	3.37	3.47	3.53	3.54	3.55	3.55	3.56
	Z	2.85	3.03	3.1	3.19	3.25	3.27	3.29	3.3	3.31
	Mean	3.1	3.2	3.29	3.39	3.43	3.45	3.46	3.46	3.47
	dVs//Fol.	0.52	0.52	0.53	0.54	0.55	0.54	0.53	0.52	0.51
1319	X	3.62	3.64	3.68	3.79	3.8	3.8	3.79	3.78	3.78
	Y	3.5	3.61	3.8	3.82	3.83	3.84	3.83	3.82	3.82
	Z	3.41	3.44	3.46	3.49	3.51	3.52	3.52	3.52	3.51
	Mean	3.5	3.56	3.64	3.7	3.72	3.72	3.72	3.71	3.7
	dVs//Fol	0.19	0.19	0.22	0.53	0.55	0.55	0.54	0.54	0.54
1335	X	3.19	3.28	3.31	3.3	3.28	3.28	3.28	3.28	3.28
	Y	3.21	3.23	3.23	3.23	3.23	3.23	3.23	3.24	3.24
	Z	3.02	3.03	3.04	3.05	3.06	3.06	3.07	3.07	3.07
	Mean	3.14	3.18	3.2	3.19	3.19	3.19	3.19	3.19	3.2
	dVs/7Fol	0.15	0.16	0.16	0.18	0.18	0.17	0.18	0.17	0.16
1349	X	2.29	2.3	2.32	2.33	2.36	2.38	2.41	2.43	2.45
	Y	2.32	2.34	2.36	2.38	2.42	2.45	2.46	2.48	2.5
	Z	2.3	2.32	2.33	2.34	2.39	2.41	2.43	2.45	2.48
	Mean	2.3	2.32	2.35	2.35	2.39	2.42	2.44	2.45	2.47
	dVs//Fol	0.18	0.18	0.18	0.19	0.19	0.18	0.18	0.18	0.18
1388	X	4.29	4.35	4.41	4.43	4.43	4.43	4.43	4.43	4.42
	Y	4.22	4.3	4.36	4.39	4.39	4.4	4.4	4.4	4.41
	Z	4.29	4.31	4.33	4.35	4.37	4.38	4.38	4.39	4.39
	Mean	4.26	4.32	4.36	4.38	4.39	4.4	4.4	4.4	4.41
	dVs//Fol	0.03	0.1	0.14	0.12	0.17	0.15	0.14	0.13	0.12

Table 6 continued

Sample	Propagation direction	25MPa	35 MPa	50 MPa	100 MPa	200 MPa	300 MPa	400 MPa	500 MPa	600 MPa
1414	X	2.27	2.29	2.29	2.3	2.33	2.34	2.35	2.37	2.39
	Y	2.34	2.36	2.38	2.39	2.42	2.44	2.46	2.48	2.49
	Z	2.22	2.23	2.24	2.25	2.29	2.32	2.34	2.36	2.38
	Meam	2.28	2.27	2.3	2.32	2.34	2.36	2.38	2.4	2.42
	dVs//Fol	0.16	0.17	0.18	0.18	0.2	0.2	0.2	0.2	0.2
1497	X	3.76	3.82	3.84	3.86	3.85	3.84	3.84	3.84	3.84
	Y	3.56	3.59	3.62	3.66	3.68	3.67	3.66	3.65	3.64
	Z	3.53	3.56	3.6	3.68	3.73	3.75	3.75	3.75	3.75
	Mean	3.62	3.66	3.69	3.74	3.75	3.76	3.75	3.75	3.74
	dVs//Fol	0.15	0.16	0.17	0.15	0.15	0.16	0.18	0.19	0.2
1658	X	3.11	3.16	3.23	3.31	3.32	3.32			
	Y	3.45	3.52	3.57	3.72	3.78	3.79			
	Z	3.29	3.35	3.42	3.51	3.54	3.55			
	Mean	3.28	3.34	3.4	3.51	3.55	3.55			
	dVs//Fol	0.19	0.23	0.31	0.36	0.39	0.37			
1844	X	2.99	3.14	3.24	3.39	3.47	3.48	3.49	3.49	3.49
	Y	2.93	3.06	3.19	3.35	3.43	3.45	3.46	3.47	3.47
	Z	2.74	2.83	2.93	3.06	3.14	3.18	3.2	3.21	3.22
	Mean	2.89	3.01	3.12	3.27	3.35	3.37	3.38	3.39	3.4
	dVs//Fol	0.74	0.67	0.66	0.66	0.66	0.66	0.65	0.64	0.63
1845	X	3.28	3.38	3.43	3.66	3.8	3.85	3.87	3.88	3.88
	Y	3.35	3.39	3.44	3.54	3.67	3.8	3.83	3.84	3.84
	Z	3.19	3.23	3.29	3.43	3.6	3.65	3.68	3.7	3.7
	Mean	3.27	3.33	3.39	3.54	3.69	3.77	3.8	3.81	3.81
	dVs//Fol	0.42	0.47	0.49	0.47	0.45	0.33	0.31	0.32	0.33

Table 7. Texture index J of major mineral in biotite gneiss

	Sample	bio	mus	qu	Plag
Upper gneiss series	OKU 578	6.49	2.71	1.18	1.77
	OKU 676	3.47	-	1.29	1.49
	OKU 818	3.47	-	1.50	1.84
	OKU 908	3.04	-	1.16	1.43
	OKU 1093	3.42	2.04	1.21	1.73
Lower gneiss series	OKU 1609	5.25	1.19	1.28	1.32
	OKU 1845	4.36	-	1.48	1.69
	OKU 2238	6.32	-	1.29	1.41

Table 8: Calculated and measured densities (ρ), Vp, acoustic impedances (I) and respective reflection coefficients (Rc) at lithologic contacts

	Calculated mean intrinsic density, velocity, impedance and reflection coefficient				**Measured mean *in situ* density, velocity, impedance and reflection coefficient**				**Measured *in situ* velocity, impedance and reflection coefficient normal to foliation**			
Lithology	**ρ g cm^{-3}**	**Vp calc kms^{-1}**	**I 10^6 kg m^{-2}s^{-1}**	**Rc**	**ρ (g cm^{-3})**	**Vp meas kms^{-1}**	**I 10^6 kg m^{-2}s^{-1}**	**Rc**	**VpZ meas kms^{-1}**	**IZ 10^6 kg m^{-2}s^{-1}**	**RcZ**	**Reflector**
Upper gneiss series												
Biotite gneiss Samples 318-1251	2.27	6.12	16.95		2.74	5.73 [1]	15.69		4.96	13.58		
				- 0.086				**- 0.085**			**-0.108**	**R1**
Meta-ophioplite												
Phlog.-graph.-gneiss Sample 1319	2.98	6.75	20.12		3.04	6.12 [2]	18.60		5.55	16.87		
				0.105				**0.145**			**0.138**	**R2**
Serpentinite Sample 1335, 1349	2.72	6.01	16.28		2.64	5.26 [3]	13.89		4.90	12.94		
				-0.203				**-0.217**			**-0.267**	**R3**
Dioside skarn Sample 1388	3.22	7.63	24.57		2.90	7.45 [4]	21.61		7.08	20.53		
				0.218				**0.254**			**0.255**	**R4**
Serpentinite Sample 1414	2.66	5.89	15.65		2.91	4.42 [5]	12.86		4.19	12.19		
				-0.096				**-0.170**			**-0.149**	**R5**
Pyr.-graph.-hbl. gneiss Sample 1497	2.79	6.80	18.97		2.86	6.32 [6]	18.08		5.75	16.45		
				0.060				**0.079**			**0.120**	**R6**
Lower gneiss series												
Biotitegneiss Samples 1609 - 1844	2.75	6.13	16.83		2.70	5.89 [7]	15.88		4.57	12.93		
				-0.113				**-0.004**			**-0.084**	**R7**
Amphibolite Sample 1845	2.88	7.33	21.11		2.88	5.84 [8]	16.82		5.31	15.29		
				0.120				**0.043**			**0.098**	**R8**
Biotite gneiss Sample 1898, 1940	2.70	6.15	16.59		2.65	6.15 [9]	15.43		4.57	12.57		
				0.0003				**-0.003**			**-0.108**	**R9**
Meta pegmatoid												
Meta pegmatoid, biotite gneiss, Samples 1940-2491	2.69	6.18	16.58		2.65	6.15 [9]	16.35		5.89	15.61		

Numbers in [ ] refer to averages of measured samples: [1] 578, 676, 818, 1093, 1319, 1335, 1349; [2] 1319; [3] 1335; 1349; [4] 1388; [5] 1414; [6] 1497; [7] 1658; 1844 [8] 1845 [9] 1658